

JPL Document D-80950

TECHNOLOGY DEVELOPMENT FOR EXOPLANET MISSIONS

Technology Milestone #1 Final Report

Visible Nulling Coronagraph Technology Maturation: High Contrast Imaging and Characterization of Exoplanets

PI: Mark Clampin (GSFC)

**VNC Team: Richard Lyon (GSFC), Peter Petrone (Sigma Space),
Udayan Mallik (GSFC), Matthew Bolcar (GSFC), Timothy Madison
(GSFC), Michael Helmbrecht (IRIS-AO)**

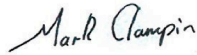
15 March 2013

National Aeronautics and Space Administration

Jet Propulsion Laboratory
California Institute of Technology
Pasadena, California

Approvals

Released by



Mark Clampin,
Principal Investigator

12/16/2013

Approved by



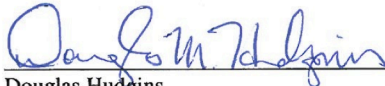
Peter R. Lawson,
Exoplanet Exploration Program Chief Technologist, JPL

12/16/2013



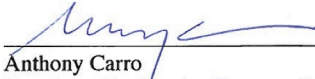
Gary Blackwood
Exoplanet Exploration Program Manager, JPL

12/17/2013



Douglas Hudgins
Exoplanet Exploration Program Scientist, NASA HQ

1/8/2014



Anthony Carro
Exoplanet Exploration Program Executive, NASA HQ

1/9/2014

Table of Contents

Executive Summary	2
1. Objective	3
2. Introduction	3
2.1. Milestone #1: Narrowband Contrast of VNC at $2\lambda/D$	4
2.1.1 Contrast: The planet-to-star contrast is defined as a ratio:.....	7
2.2. Visible Nulling Coronagraph	11
2.2.1 Description of Flight VNC	12
2.2.2 Description of Lab VNC	13
2.2.3 VNC Technologies	18
2.3. Error Budgeting & Traceability of Lab Demonstration to EPIC	21
2.3.1 Basis of Error Budgeting Formalism	21
2.3.2 Description of Error Budgets.....	23
2.3.3 VNC Point Spread Function and Plate Scale	26
2.3.4 Design of VNC Diagonal Wavefront Control Modes	29
2.3.5 Validation and OSCAR Modeling	33
2.3.6 Difference Between Flight VNC and Lab Vacuum Nuller.....	35
3. Milestone Procedure	36
3.1. Top-Level Description	36
3.2. Detailed Description	39
3.3. Focal Plane Contrast Measurement Steps	42
3.4. Milestone Validation Procedure	45
4. Success Criteria	47
5. Results	48
6. Certification Process	53
6.1. Milestone Certification Data Package	54
7. Summary and Future Milestones	55
8. Glossary	56
9. References	58

Executive Summary

We describe the technology maturation of the visible nulling coronagraph to achieve milestone #1 (*Section 2.1*), which definitively demonstrates $<10^{-8}$ contrast at an inner working angle of $2 \lambda/D$ to greater than 90% confidence in narrowband ($<1\%$) light. The success criteria are described in *Section 4* of the report, and the results, with supporting evidence, are described in *Section 5*, and summarized in *Table-5*.

The descriptions herein include the: (i) layout and description of the VNC testbed (*Section 2.2.2*), (ii) error budgeting (*Section 2.3.1 and 2.3.2*), (iii) calibration of the plate scale to map the high contrast camera image to angular units in terms of λ/D (*Section 2.3.3*), (iv) overall wavefront control approach (*Figures 18, 19, 20 and 21*), with significant detail for the final fine control (*Section 2.3.4*), (v) description of the contrast metric used to achieve milestone #1, (vi) finally we show significant implementation details and convincing performance evidence that the milestone has been achieved (*Section 5 and Table-5*).

TDEM Milestone Report:

Visible Nulling Coronagraph Technology Maturation

1. Objective

In support of NASA's Exoplanet Exploration Program and the ROSES Technology Development for Exoplanet Missions (TDEM), this report describes the accomplishment of TDEM Milestone #1 for the *Visible Nulling Coronagraph* of the Extrasolar Planetary Imaging Coronagraph¹ (EPIC). It delineates how the flight requirements are traced down to this milestone and specifies the quantitative and empirical methodology for evaluating the milestone, and the success criteria against which the milestone will be judged. It furthermore presents experimental results and documents the completion of the milestone.

2. Introduction

This Technology Milestone serves to gauge the developmental progress of the critical technology for a space-based exosolar planetary mission, such as EPIC (Figure-1) (Clampin, 2009), that would detect and characterize exoplanets and dust and debris disks, and the mission's readiness to proceed from pre-Phase A to Phase A. Completion of this milestone is documented in this report by the Principal Investigator and reviewed by NASA HQ. The completion of the first milestone addressed herein is for visible light narrowband nulling coronagraphy to accomplish focal plane starlight suppression. The approach utilized the GSFC Vacuum Nuller testbed with adaptive null control, with lateral beam shear, and a narrowband spectral bandpass as Milestone #1. Later milestones will proceed to deeper contrasts (Milestone #2), and broadband (Milestone #3). The primary differences between Milestone #1 and #2 is the incorporation of spatial filter array (SFA) to allow deeper contrast. The difference between Milestone #2 and #3 is the introduction of achromatic phase control allowing broader band contrast. Only accomplishment of milestone #1 is described herein and Milestones #2 and #3 are briefly described in section 6 on 'Future Milestones'.

The proposed EPIC flight mission's telescope (Figure-1 left panel) couples planet- and star-light into a visible nulling coronagraph (VNC) (Figure-1 yellow box on bottom of left panel), and shown expanded in Figure-1 middle panel. The VNC suppresses starlight relative to planet-light thereby increasing the contrast of the planet to the star. The critical technologies are the two nullers (orange benches in the center and on right wall of the housing in middle panel of Figure-1). A single nuller (Figure-1 right panel) is a modified Mach-Zehnder shearing interferometer that splits the light into two paths such that the on-axis starlight light is cancelled, or nulled, and the off-axis planet light transmits at periodically spaced transmission maxima. *Milestone #1 addresses the most stressing technology advancement for a single nuller only.*

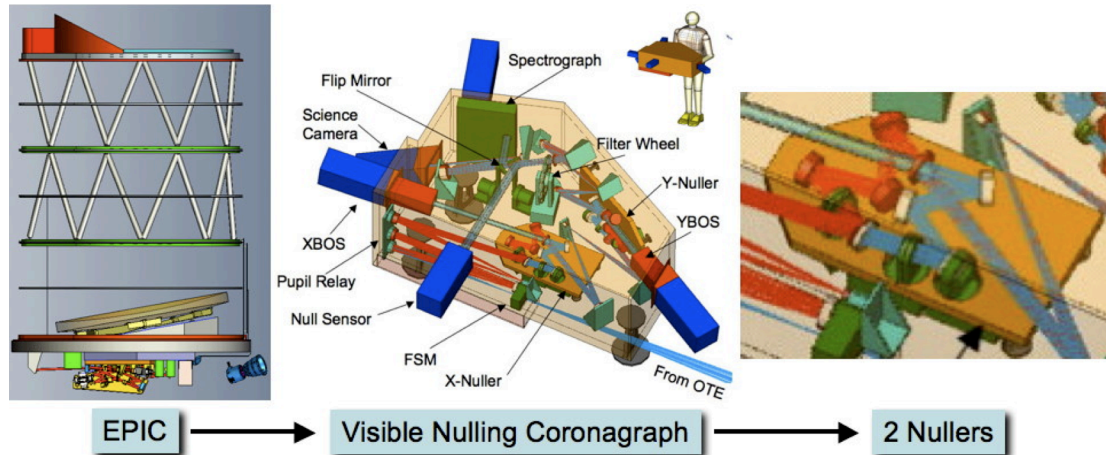


Figure-1: *Extrasolar Planetary Imaging Coronagraph (EPIC)*

A (left panel) proposed flight mission with an unobscured Cassegrain telescope feeding light into the visible nulling coronagraph (yellow box bottom of left panel), shown expanded (middle panel). The VNC suppresses the starlight relative to the planet-light and thereby increases the contrast of the planet to star. The critical technologies are the two nullers (orange benches in the center and on right wall of housing in middle panel). A nuller (right panel) is a modified Mach-Zehnder shearing interferometer and Milestone #1 addresses advancement of a single nuller and its associated technology.

2.1. Milestone #1: Narrowband Contrast of VNC at $2\lambda/D$

Demonstrate that the Visible Nulling Coronagraph (VNC) can achieve and hold a contrast of 1×10^{-8} (goal less than 1×10^{-9}) at a $2\lambda/D$ inner working angle at a visible wavelength centered in a narrowband filter of spectral bandpass $< 1\%$.

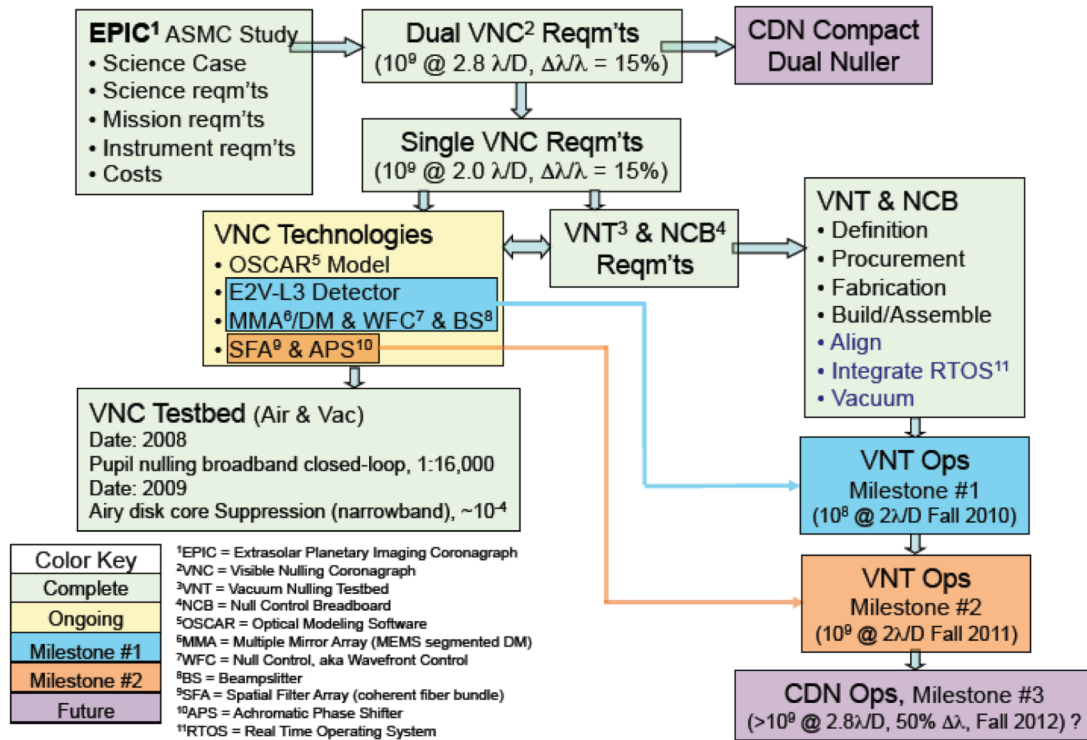
Milestone #1 demonstrates traceability to three of the key EPIC requirements of: (1) contrast of 10^{-9} , (2) at an inner working angle (IWA) of $2\lambda/D = 125$ mas, (3) with a stability time of 1000 seconds. The specific milestone criteria are:

- 1) Illumination is narrowband light ($< 1\%$ spectral bandpass) in a single linear polarization at a wavelength centered on 632.8 nm.
- 2) The mean plus 1.33 of the standard error of the contrast is 1×10^{-8} or smaller at a pixel at $2\lambda/D$, as reported in a Data Collection Event (DCE) spanning 1000 seconds of continuous data-taking containing 200 contrast estimates reported as a function of time.
- 3) The milestone requires that elements 1 & 2 must be satisfied on three separate occasions with at least 24 hours between the beginnings of each demonstration.

These requirements are all allocated within the EPIC top-level error budget, (Section 2.3.2) flowed to the VNC error budget and to the error budget for a single nuller. In Figure-2 we show the context for Milestone #1 and how it is derived from the requirements of the EPIC mission concept (Clampin 2009). Components of EPIC's error

budgets were derived and assessed by thermal/structural/optical modeling (STOP), and this includes the optical telescope element (OTE) and VNC. EPICs error budgets were used to set requirements for and derive error budgets for the lab VNC milestone and are

Figure-2: Linkage of EPIC's science requirements to TDEM milestone, and previous VNC technology milestones.



further discussed in section 2.3.2. The flight VNC consists of two “nullers” in series, while the lab VNC consists of a single “nuller”. A nuller is the modified Mach-Zehnder interferometer per the rightmost panel of Figure-1 (orange breadboard) and shown in Figure-5 and described in sections 2.2.1 (for flight) and 2.2.2 for the lab VNC.

The to be described successful completion of Milestone #1 builds increasing confidence that the modeling and error budget correlates with measured observables within the VNC ground laboratory environment, and that the physics of nulling is well understood and there are no engineering issues that represent a ‘dead end’ development path. However, milestone #1 does not attempt to match all requirements for EPIC since this is outside of the current scope of this effort. Requirements for spectral bandpass ($>20\%$) and flight contrast of $<10^{-9}$ are not within the scope of Milestone #1: however, these are delineated as future milestones. Additionally, since the VNC is modular in design, Milestone #1 addresses a single VNC nuller, i.e. the flight VNC contains two nullers (dual nuller) in series. System-level milestone demonstrations for the dual nuller are relegated to the future.

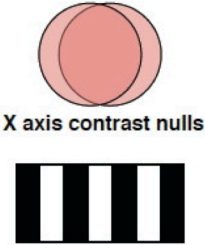
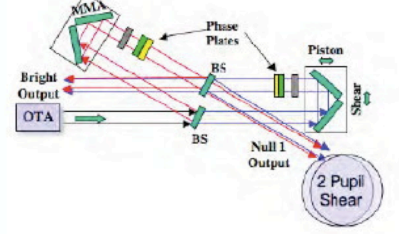
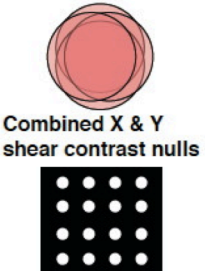
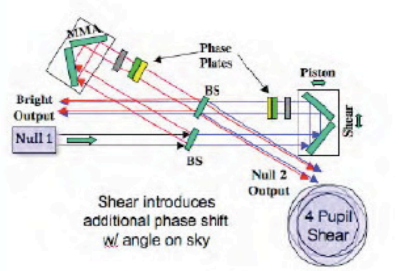
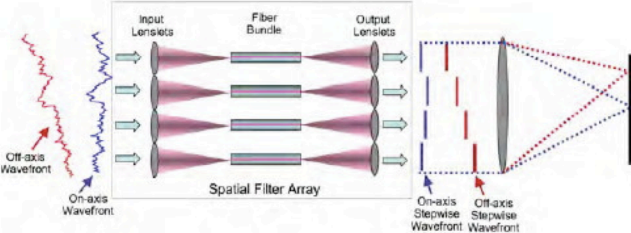
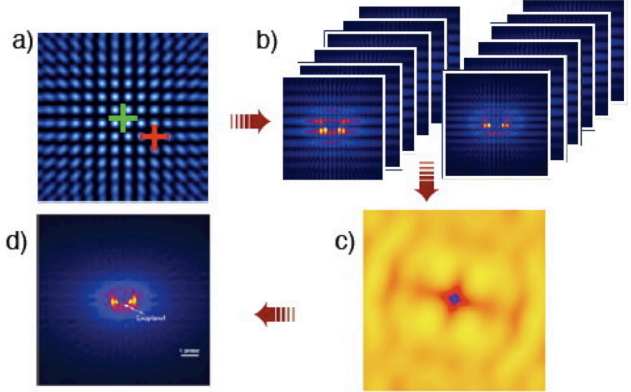
Optical Outputs	VNC stage	Comments
<p>Pupils sheared in X</p>  <p>X axis contrast nulls</p>	<p>First nuller stage</p> 	<p>First Nuller Stage</p> <ul style="list-style-type: none"> •The first stage of the VNC shears the telescope pupil in the X axis by means of a shearing interferometer arm • The output is fed to the second nulling stage • The bright output (BS) is used for pointing and WFSC
<p>Pupils sheared in Y</p>  <p>Combined X & Y shear contrast nulls</p>	<p>Second nuller stage</p> 	<p>Second Nuller Stage</p> <ul style="list-style-type: none"> •The second stage of the VNC shears the input from the first nuller stage in the Y axis by means of a shearing interferometer arm • The output is fed to the spatial filter array • The bright output (BS) is used for WFSC
 <p>Spatial Filter Array (SFA)</p>	<p>Spatial Filter Array (SFA) The SFA removes high frequency components from the nulled wavefront and comprises an array of fibers interfaced to a lenslet array at each end.</p>	
	<p>VNC discovery observation sequence:</p> <ol style="list-style-type: none"> Pattern of contrast nulls projected on the sky. The green cross shows the location of the star at a null. Observation sequence builds the null on the sky by combining 12 images obtained at 4 shears and 3 telescope rolls Effective null pattern on the sky produced by sequence (b) Actual science image when the parent star is nulled to reveal an exoplanet. <p>VNC characterization mode simply places planet so it falls in a contrast maximum [red cross in (a)] Note: binaries are observed by placing both stars in a null minimum</p>	

Figure-3: Principal of Visible Nulling Coronagraph

The definitions of contrast and inner working angle within Milestone #1 are more clearly explained with regards to the VNC after an explanation of how the VNC suppresses starlight.

The VNC consists of two nullers in series as shown in the middle panel of Figure-1. Figure-3 shows the operating principle behind the VNC. The 1st nuller shears in X and the 2nd in Y; shearing is the lateral translation (across the beam diameter) of one beam

relative to another. Shearing in X gives an off-axis phase shift that varies with field position on the sky as shown schematically as the alternating black and white pattern projected on the sky in the upper left inset of Figure-3; this pattern is termed the VNC's transmission function. A star on a black bar would not transmit through to the science detector while a planet on a light bar would transmit through to the science detector. Shearing the output again in Y results in the transmission function shown as the pattern of alternating spots in the 2nd left inset down from the top of Figure-3. In reality the sky transmission pattern is not opaque where black or fully transmitting where white; its actual form is shown in figure-a in the lower left inset of Figure-3. Increasing the amount shear (i.e. translating one arm of the interferometer relative to the other) results in a pattern of spots that are closer together and conversely further apart for less shear. Shear results from lateral translation of one of the nuller arms relative to the other; zero shear implies that the beams perfectly overlap. Changing the shear and the pupil roll (i.e. optically rolling the pattern about the star) gives a sequence of transmission functions shown as Figure-b. Co-adding the transmission functions gives an aggregate transmission function shown as Figure-c in the lower left inset of Figure-3, where light colors represent higher transmission and dark colors (as in the center) represent minimal transmission. Thus a high contrast image can be built up from a sequence of shears and rolls (Figure-d), or for exoplanets at known sky locations the shear and roll can be set to optimize planet to star contrast at that location in sky.

If the planet location is unknown then a shear and roll search must be used (discovery mode), however, if the planet location is known then the shear and roll can be optimally tuned to set a maximum of the transmission pattern at the location of the planet and spectroscopy performed (characterization mode). Additional optimization schemes for observing can be envisioned where, for example, small shears are initially used to search for planets at larger orbital radii from the star with increasing shear moving the IWA closer to the star.

2.1.1 **Contrast:** The planet-to-star contrast is defined as a ratio:

$$C = \frac{N_{\lambda:PLANET}}{N_{\lambda:STAR}} \quad (1)$$

Where $N_{\lambda:PLANET}$ and $N_{\lambda:STAR}$ are the aperture irradiances (photons/sec/meter²/micron) of the planet and star respectively. The product of either $N_{\lambda:PLANET}$ and $N_{\lambda:STAR}$ with the sheared aperture collecting area, spectral bandpass, throughput and quantum efficiency gives the spatially integrated photoelectron rates in the focal plane and thus the observed contrast as:

$$C = \frac{\int d\lambda \int d\Omega [N_{\lambda:PLANET} \times f_{SHEAR} \Delta A \times T_O \times q.e.]}{\int d\lambda \int d\Omega [N_{\lambda:STAR} \times f_{SHEAR} \Delta A \times T_O \times q.e.]} \quad (2)$$

The integrals are taken over the solid angle ($d\Omega$) subtended by a single pixel of the detector focal plane centered on the star in the denominator, and centered on the planet in the numerator, and over the bandpass of interest ($d\lambda$). Note that this definition ignores

zodiacal and exozodiacal light and treats only the flux from the planet and star and nothing else within the field-of-view of the detector. Additionally it is possible to weight the irradiance prior to summing over a region of detector pixels, e.g. as in a matched filter or sharpness metrics; weighted approaches are not addressed herein and within this effort we work with the raw unprocessed contrast as defined by equation (2).

A planet that is e.g. 9 orders of magnitude dimmer than its parent star would yield a contrast as defined above of 10^{-9} . The purpose of the VNC is to increase the ratio of the planetary-to-stellar flux such that after passing through the VNC the ratio of the planetary flux (as measured at the planet's location) to stellar flux (but measured at the planet's location) is unity or greater when integrated over a region of the focal plane defined by a detector pixel.

True measurement of contrast requires both the star and planet, however in the lab VNC only a single source is used; contrast is inferred from detector measurements of how dark the VNC is, i.e. how much suppression is measured as a function of focal plane location. Thus during the lab measurement process the integral in the numerator of equation-2 is evaluated after control has adjusted the system to minimize the counts due to the star at the planets position, while the integral in the denominator is evaluated after control has adjusted the system to maximize the counts at the stars position.

2.1.2 Inner Working Angle

The smallest planet-to-star angular separation at which the required contrast is achieved is defined to be the inner working angle. Figure-3 lower left inset showed an illustration of the high contrast imaging process with a VNC. This transmission pattern for a single roll (roll angle 0^0) and shear (0.25 pupils) is shown in the left panel of Figure-4. The x- and y-axis are angles on the sky and the transmission pattern takes the functional form:

$$T(\theta_x, \theta_y) = \sin^2\left(\pi \frac{s_x D}{\lambda} \theta_x\right) \sin^2\left(\pi \frac{s_y D}{\lambda} \theta_y\right) \quad (3)$$

Where (θ_x, θ_y) are the sky angles, λ and D are the wavelength and beam diameter ($D=1.65\text{m}$ for EPIC) respectively and (s_x, s_y) are the fractional lateral beam shear in the x- and y-directions respectively, in units of beam diameters. Pointing the telescope such that the star falls on the center of the transmission pattern (red cross-hair in left panel of Figure-4) effectively *nulls* the starlight since $T(0,0)=0$, and where *null* refers to destructive interference. Conservation of energy requires that the starlight passes through the VNC but it exits at the bright output channel and is used for pointing and wavefront control (discussed in sections 2.2 and following). Setting the shear and/or rolling the spacecraft, or optically rolling the transmission pattern on the sky, such that the planet is on a transmission maximum (bright peaks in left panel of Figure-4) transmits (constructively interferes) the planet light allowing it to pass through to the dark science focal plane detector.

Varying the shear and rolls allows an extended scene image to be constructed of an exoplanet system as shown in the right panel of Figure-4. One approach to constructing image without errors consists of co-adding the combinations of shear and rolls:

$$I(\theta_x, \theta_y) = \sum_j PSF_j(\theta_x, \theta_y) ** [T_j(\theta_x, \theta_y) O(\theta_x, \theta_y)] \quad (4)$$

Where $PSF_j(\theta_x, \theta_y)$ is the optical point spread function (PSF) of the telescope at the j-th shear/roll combination, $T_j(\theta_x, \theta_y)$ is the sky transmission function at the j-th shear/roll and $O(\theta_x, \theta_y)$ is the object, and $**$ denotes 2-dimensional convolution, and the sum is taken over the set of shear and roll combinations. Equation (4) is shown visually as a simulation of our solar system placed at 10 pc in the right panel of Figure-4 on a square-root color scale (color bar on bottom) and is in units of photoelectrons/pixel/second without noise. Integrating this over a time window with noise effects would yield a simulation of an observed EPIC image with 12 combinations of roll and shear.

Once the planet location is known, e.g. Jupiter in Figure-4 right panel, the shear/roll can be optimally tuned to maximize planet transmission and spectroscopy performed.

The 1st transmission maximum ($T=1$) occurs at $(\theta_x, \theta_y) = (1/s_x, 1/s_y) \frac{\lambda}{2D}$ and is denoted as the inner working angle (IWA). For a lateral shear of 0.25 beam diameters, first in X and then in Y, the $IWA = 2.8\lambda/D$ where λ is the central wavelength in the bandpass.

Achievement, with the lab VNC emulating a single nuller of the VNC, of both the contrast and the IWA necessitates both lateral beam shear by 25% of the input beam diameter, and wavefront sensing and control at that beam shear to achieve 10^{-8} at $2\lambda/D$. In the lab VNC, visually a dark hole will be evident in the focal plane images in the region surrounding the IWA and it is the depth of this dark hole that will be measured relative to the brightness of the core of an unsuppressed unresolved image as functions

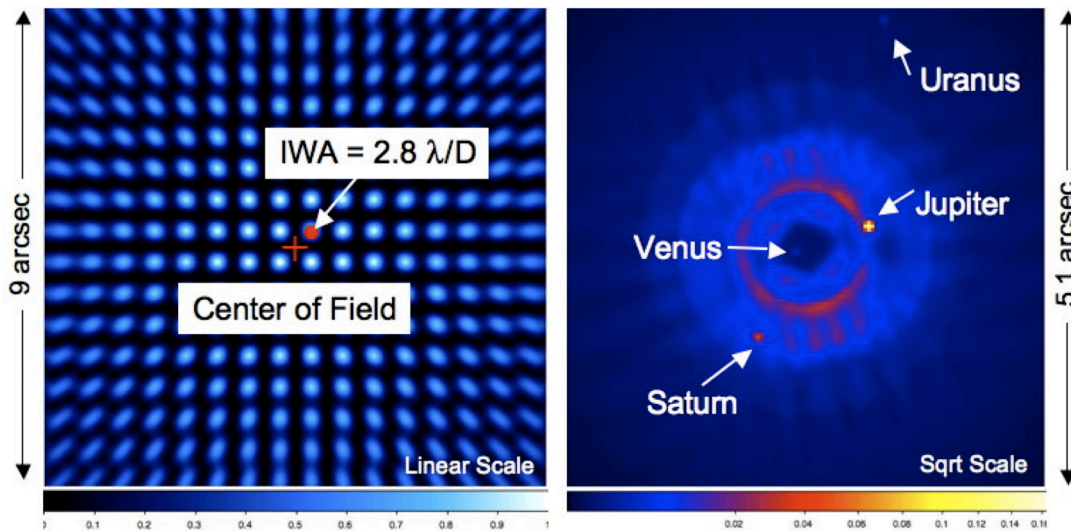


Figure-4: Left: *Sky Transmission Pattern* w/ 10% bandpass for a single shear/roll shown over a FOV of 9 arcseconds square on linear scale - red cross-hair is central null. Right: *Simulated Face-on Solar System Image @ 10 pc* consisting of co-adding 12 shear/roll combinations with 10% bandpass over a FOV of 5.1 arcseconds square. Image on square-root color scale, units of photoelectrons/sec/pixel without detector noise. Simulated with a sequence of 12 shear/roll combinations using as input a dust/debris disk simulation by Stark & Kuchner (2008) with planets added.

of: time, focal plane location and shear for a broadband source with a narrowband spectral filter.

2.1.3 Stability

The mean of the contrast ratio was maintained at, or better than 10^{-8} , for > 1000 seconds and ensures that sensing and control is adequate to maintain contrast, and that it is not a spurious result. 1000 seconds was chosen to be scalable and traceable to flight observing time windows for both detection and spectroscopic characterization.

2.1.4 Discussion of Milestone #1

Milestone #1 addresses several key aspects of the EPIC performance error budget. EPIC is required to form a high contrast “dark field” over a working angle spanning $2 - 16 \lambda/D$, over a spectral range of 480 to 960 nm. The contrast at an IWA of $2\lambda/D$ is driven primarily by differences in the wavefront error between the two arms of the VNC at 2 cycles per aperture (cpa). At this spatial frequency the spatial wavefront structure is mainly caused by near-common path errors from the OTE, and from non-common path errors introduced in the arms of the VNC. Uncontrolled spatial frequencies at ~ 2 cpa will limit contrast at EPIC’s inner working angle of $2\lambda/D$. *The 1st milestone addresses contrast at the most challenging focal plane location ($2\lambda/D$), and is directly traceable directly to a flight requirement in the EPIC Astrophysics Strategic Mission Study (Clampin, 2009).*

In order to achieve this IWA of $2\lambda/D$, the VNC’ internal lateral beam shearing must be set to $\frac{1}{4}$ of the beam diameter, and the wavefront spatial frequencies at ~ 2 cpa must be sensed and controlled in closed loop to hold the mean contrast at 1×10^{-8} (90% confidence limit). The milestone demonstrates that the mean contrast can be held for > 1000 seconds, a stability requirement that traces to the exposure times required to search, detect, and perform spectroscopic characterization of exoplanets. Conclusion of this milestone also validates the VNC sensing algorithms employing the bright and dark outputs, and the control algorithms for the multiple mirror array (MMA). The repeatability component of the milestone’s requirements demonstrates that the result can be repeated, and emulates a slew to a new target for the flight mission.

The outer working angle (OWA) is achieved using a large (at least 925 segment) MMA, with piston, tip, and tilt control on each MMA segment. A segmented MMA with this format is not yet available and so the lab VNC addressed a localized region extending from an IWA of $2\lambda/D$ out to an OWA of $\sim 5 \lambda/D$. This is sufficient to show that the wavefront control problem can be addressed with high expectation of applying the same approach to a larger dark field at a later date.

It is expected that the flight VNC would cover the 480–960 nm spectral range in a series of discrete photometric bands each of $\sim 20\%$ and each of these discrete bands is referred to herein as “instantaneous spectral bands”.

EPIC must be capable of detecting light reflected by a planet with intensity 10^9 fainter than that of the parent star. Ideally this is achieved by driving all diffracted/scattered light surrounding the star to an intensity contrast ratio of diffracted/scattered light to parent starlight below 10^{-10} . In pre-Phase A, the VNC is expected to demonstrate contrast reduction to the 10^{-9} level via a series incremental Milestones: Milestone #1 (narrowband and 10^{-8}) as described herein, and Milestone #2 (narrowband but 10^{-9}) and Milestone #3 ($<10^{-9}$ broadband). Milestones #2 and #3 are described in follow-on documents. By achieving these results, VNC will have ultimately demonstrated performance that is limited not by the instrument but by the nature of the target.

Uncontrolled speckles in the high contrast focal plane region are statistically distributed with a long-tailed negative exponential probability distribution such the mean intensity at a given location is equal to the standard deviation at that same location. This implies that while dark speckles are more likely there will also be bright speckles with lower probability. Our error budgeting formalism is based on the mean speckle intensity plus 3-sigma which gives a tighter requirement than just using the average speckle contrast. However we adhere to the more standardized formalism of using 90% confidence limits for assessment of the contrast milestone. Using 90% confidence limits effectively gives relaxed tolerances within the error budget; this is treated as margin in the flight design.

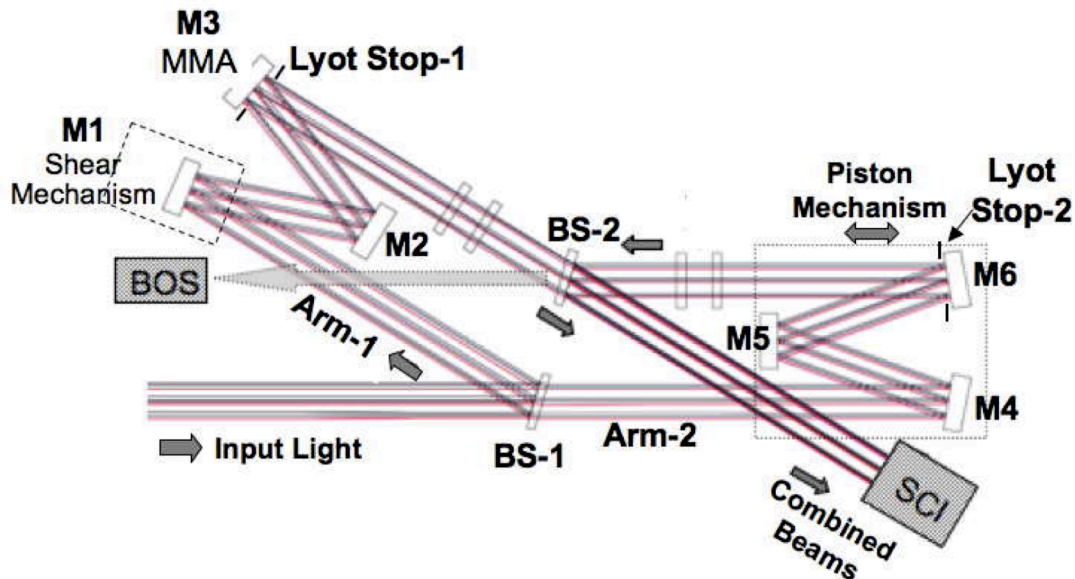


Figure-5 – Code-V Optical Layout of Single Nuller for Milestone #1

2.2. Visible Nulling Coronagraph

Critical to understanding Milestone #1 is how the flight VNC and lab VNC work and what their differences are. The VNC was conceptually described in section 2.1 and a more detailed description follows herein.

2.2.1 Description of Flight VNC

The EPIC flight VNC consists of two nullers in series as shown in Figure-1. Light from the optical telescope element (OTE) enters and passes through a relay with a fine steering mirror and enters the 1st nuller (orange 6-sided optical bench near center of middle panel of Figure-1). The 1st nuller has both a bright and dark output; the dark output is relayed to the 2nd nuller (orange 6-sided optical bench on the right wall, while the bright output is used for pointing and wavefront control. Each flight nuller is a modified Mach-Zehnder interferometer with the Code-V optical design shown in Figure-5. The input light is 50:50 split by beamsplitter-1 and passes through the two arms (arm-1 and arm-2). Arm-1 reflects off the 1st beamsplitter while arm-2 transmits. In arm-1 the beam reflects from 3 flat optics (M1, M2, M3) of which M1 is mounted on a shear mechanism that moves in 1 degree of freedom (DOF) normal to the incoming beam. The shear mechanism laterally translates the beam in arm-1 relative to arm-2. M2 folds the beam onto the Multiple Mirror Array (MMA) (mirror M3), discussed in section 2.2.3, at near normal incidence. Herein we refer to the hexagonal packed segmented deformable mirror as the MMA to differentiate it from continuous facesheet deformable mirrors since the MMA does not actually deform. After the MMA, the beam both reflects and transmits off beamsplitter-2, and beamsplitter-2 is matched to the transmission/reflection characteristics of beamsplitter-1. The reflected beam passes out to the bright object sensor (BOS) and the transmitted to the science output (SCI). The high contrast science output is the dark output, and when nulled, most of the light passes to the BOS. The light that transmits through beamsplitter-1 also reflects off fold flats M4, M5 and M6 as shown to the right of Figure-5. M4, M5 and M6 are all mounted on a single 1-degree of freedom (DOF) two-stage actuation assembly (piston mechanism) that moves to maintain the mean phase

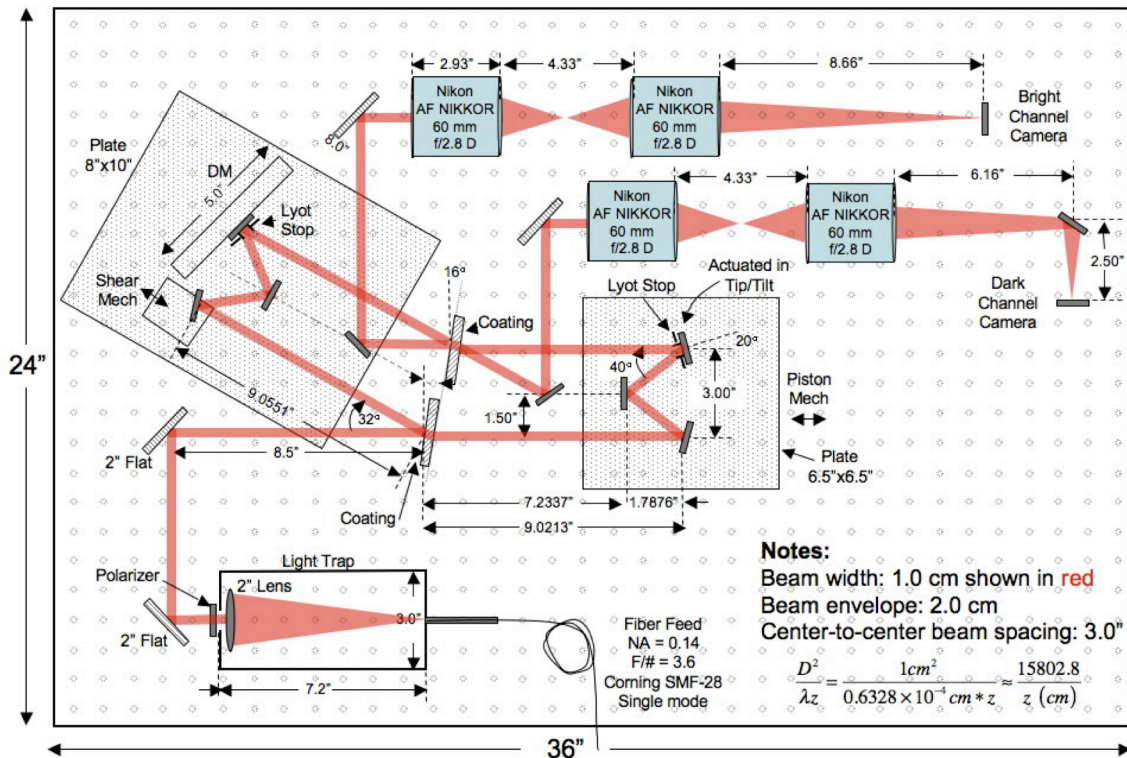


Figure-6: Diagram of Vacuum VNC for Milestone Achievement

difference between arm-1 and arm-2 at π radians at the center wavelength. Light from arm-2 also transmits and reflects off beamsplitter-2 and is mixed against the beams from arm-1. Just in front of the MMA and its counterpart in arm-2 are pupil stops 1 & 2 that are matched to each other and to the pattern of the MMA and ensures that the Fresnel diffraction within the two arms matches. At the output of the bright and dark arms are relay optics (not shown) that relays the beams onto the bright and dark detector arrays. For the flight nuller the dark output is collimated and relayed to the 2nd nuller. This 2nd nuller is a duplicate of the first except it is rotated 90 degrees relative to the output beam from the 1st nuller.

2.2.2 Description of Lab VNC

The Lab VNC was designed to emulate the optics and sensing and control of a single nuller of the flight VNC. It also has both a bright (WFC) and dark output channel (for contrast assessment) and is shown schematically in Figure-6, an annotated photo of it in Figure-7, and map (indexed to Table-1) to the relevant components in Figure-8. Relay optics, on the output bright and dark channels, relays the images onto the detectors. The lab VNC is built on a 36"x24"x5" optical breadboard that is moved into and out of a vacuum tank using a lift (Figure-9). Outside the tank it rests on the staging airtable, while in the tank it rests on passive isolators on a shelf in the vacuum tank. The vacuum tank rests on a 1-Hz air table with passive isolators under the feet of the vacuum tank as shown schematically in Figure-9 (right) and this facility resides in the new NASA/GSFC Building 34 lab facility. During measurements the entire table is floating and measurements with thermistors have shown that the temperature within the tank stabilizes in ~20 minutes. Vacuum feedthroughs pass through two tank bulkheads, one on either side, and the feedthroughs consist of optical fiber feedthrough, electrical feedthroughs, and water chiller feedthroughs for camera cooling. Additionally a master heat strap resides within the tank. This facility is what was used to achieve the milestone, and has seen use for nulling with the 1st generation VNC testbed (Lyon 2010).

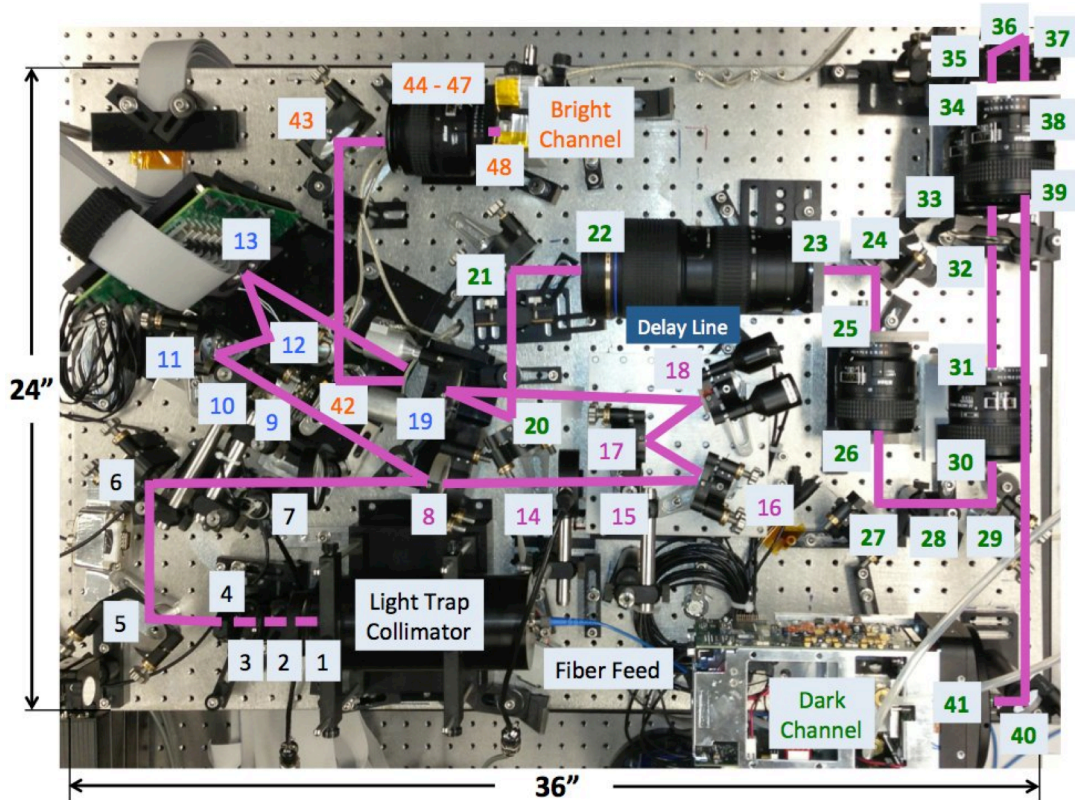


Figure-7: Annotated Photograph of Lab VNC. Numbers refer to optical element index in column 2 of Table-1 (below) and color code refers to each sub-system.

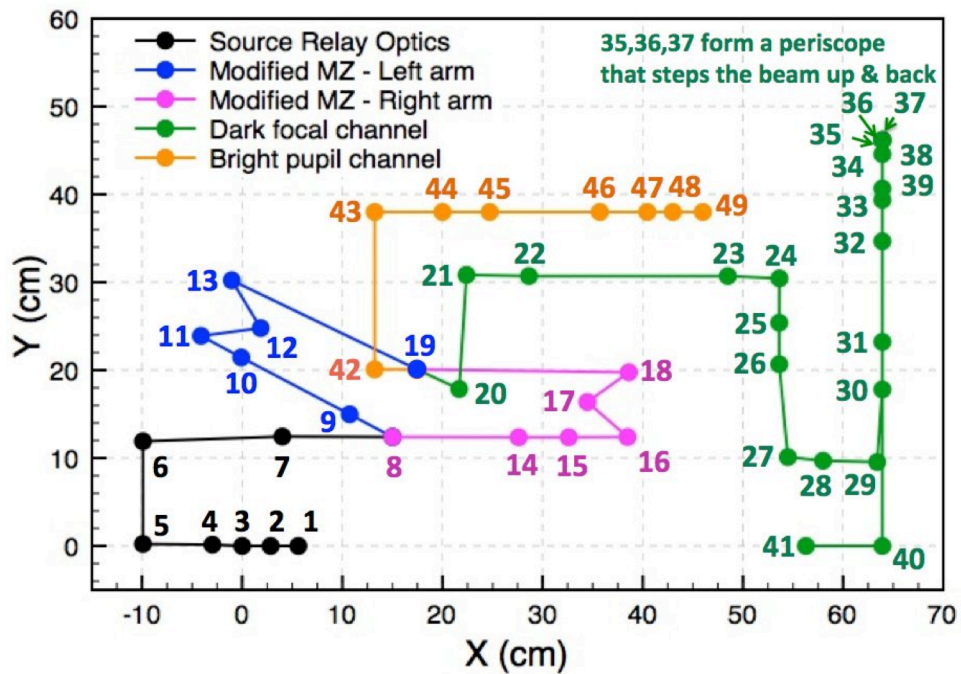


Figure-8: Numbered layout of VNC. Numbers refer to optical element index in column 2 of Table-1 (below) and color code refers to each sub-system.

Table-1: Relevant Optical Parameters (each component is shown on Figure-8)

Sub System	#	Element Name	X (cm)	Y (cm)	Z (cm)	Beam Diam (mm)	Element Description
Source Relay Optics	1	Aperture	5.61	0.00	10.16	10.00	Source Module Aperture
	2	2" Lens	2.84	0.00	10.16	10.00	Bi-Convex Lens , Reimage Pupil 1:1
	3	Iris	0.00	0.00	10.16	8.80	Reference Datum (0,0) for system
	4	Polarizer #1	-2.97	0.15	10.16	6.20	Establishes Vertical-Pol
	5	1 st 2" Fold	-9.91	0.23	10.16	6.00 X 4.50	2" Fold Flat
	6	2 nd 2" Fold	-9.91	11.91	10.16	6.30 X 4.00	2" Fold Flat
	7	Pupil Lens	4.01	12.45	10.16	10.00	Bi-Convex Lens , Reimage Pupil 1:1
Modified Mach-Zehnder	8	BS #1	15.01	12.40	10.16	10.00	Input face of BS
	9	Shutter #1	10.73	14.98	10.16	10.00	Uniblitz shutter
	10	Polarizer #2	-0.09	21.45	10.16	10.00	Mitigates cross leakage
	11	Shear W Flat 1	-4.11	23.90	10.16	10.00	1 st one inch dia flat in shear "W"
	12	Shear W Flat 2	1.85	24.79	10.16	10.00	2 nd one inch dia flat in shear "W"
	13	Deformable Mirror	-1.04	30.23	10.16	10.00	Deformable Mirror
	14	Shutter #2	27.61	12.37	10.16	10.00	Uniblitz shutter
	15	Polarizer #3	32.61	12.37	10.16	10.00	Polarizer for DL leg (mitigates leakage)
	16	DL, Flat #1	38.48	12.40	10.16	10.00	1 st one inch dia flat in delay line "W"
	17	DL, Flat #2	34.47	16.38	10.16	10.00	2 nd one inch dia flat in delay line "W"
	18	DL, Flat #3	38.61	19.76	10.16	10.00	3 rd one inch dia flat in delay line "W"
19	BS #2	17.45	20.09	10.16	10.00	Incident Face (opp face than BS1)	
Dark Focus Channel	20	1 inch Fold	21.67	17.86	10.16	10.00	Fold feeds 2" Fold Before Tamron Lens
	21	2" Fold	22.40	30.84	10.16	10.00	Fold in front of Tamron Zoom lens
	22	Tamron Input	28.63	30.71	10.16	10.00	Objective of Tamron Zoom
	23	Tamron Output	48.49	30.71	10.16	2.10	Center of rear lens, Tamron Zoom
	24	1" Fold	53.64	30.45	10.16	3.50 X 2.50	Feed mirror, Tamron to Nikon
	25	Nikon Lens #1 (In)	53.62	25.40	10.16	6.50	Surface of Input element, Nikon lens #1
	26	Nikon Lens #1 (Out)	53.62	20.68	10.16	8.00	Surface of output element, Nikon lens #1
	27	1" fold Mirror	54.48	10.11	10.16	1.00	Fold after Nikon Lens #1
	28	Polarizer #4	57.99	9.70	10.16	2.30	Measurement at input face
	29	1" Fold	63.40	9.55	10.16	6.20	Fold after Polarizer
	30	Nikon Lens #2	63.91	17.81	10.16	10.00	Input side
	31	Nikon Lens #2	63.91	23.22	10.16	7.50	Lens that feeds Lyot Stop
	32	Lyot Stop	63.91	34.67	10.16	10.00	Estimate, center face of Lyot Stop
	33	Nikon Lens #3 (In)	63.91	39.37	10.16	-	Feeds lower fold mirror in periscope
	34	Nikon Lens #3 (out)	63.91	44.58	10.16	10.50	Feeds lower fold mirror in periscope
	35	Lower Periscope Fold	63.91	46.18	10.16	7.80 X 10.50	Lower Fold, Periscope
	36	Diverging lens	63.91	46.18	13.69	2.45	Input face of div lens, lower surface
	37	Upper Periscope Fold	63.91	46.18	18.34	2.50	Upper Fold, Periscope
	38	Nikon Lens #4 (In)	63.91	46.18	18.24	4.25	Upper Nikon lens
	39	Nikon Lens #4 (out)	63.91	40.67	18.24	5.50	Upper Nikon lens
	40	1" Fold Flat	63.91	0.00	18.24	near focus	45 degree flat to fold beam into EMCCD
41	Dark Channel Camera	56.29	0.00	18.24	focus	Science camera	
Bright Pupil Channel	42	1" Flat	13.23	20.09	10.16	-	1st fold flat for bright channel pupil image
	43	2" Flat	13.23	38.00	10.16	-	2nd fold flat for bright channel pupil image
	44	Nikon Lens #5 (in)	20.00	38.00	10.16	-	front surface of 1st lens of pupil relay
	45	Nikon Lens #5 (out)	24.72	38.00	10.16	-	back surface of 1st lens of pupil relay
	46	Nikon Lens #6 (in)	35.72	38.00	10.16	-	front surface of 2nd lens of pupil relay
	47	Nikon Lens #6 (out)	40.44	38.00	10.16	-	back surface of 2nd lens of pupil relay
	48	Polarizer #5	43.00	38.00	10.16	10.00	Removes cross-leakage
	49	Pixelink	46.00	38.00	10.16	10.00	Bright Channel pupil image for WFC

The Lab VNC is the 2nd generation one developed by our group, along with a white light Michelson nulling interferometer for testing various MMAs and fiber bundles. It consists of supercontinuum broadband source module with an array of spectral filters. This source consists of a laser pumping a photonics fiber which through a series of nonlinear effects broadens the spectrum to approximate a blackbody but with 10^4 - 10^5 times more radiance over the spectral range of $\sim 500 - 2400$ nm. For milestone #1 we used a narrowband HeNe filter centered at 633 nm since high rejection filters exist at this bandpass. Light from the supercontinuum source fiber passed through the spectral filter and selected ND

filters and is fiber injected outside the tank to mitigate stray out-of-band light. The supercontinuum source resides off the air table to minimize vibration from its cooling fan; the source fiber output end, narrowband filter and feedthrough fiber input end are encased in a shroud to minimize any stray out-of-band light from coupling into the tank from stray sources in the room outside the tank.

Nomenclature and Terminology: The layout of the lab VNC is as illustrated in Figure-6 and shown with the optics labeled in Figures 7 and 8. Table-1 and Figures 7,8 are complementary in that the numbered, color-coded closed circles on Figures 7,8 refer to the list of elements in Table-1. The font color is different for the subsystems labeled in the legend of Figure-8. The subsystems are *Source Relay Optics* (black), *Modified MZ – left arm* (blue), *Modified MZ – right arm* (magenta), *Dark focal channel* (green), and *Bright Pupil Channel* (orange). “Modified MZ” refers to modified Mach-Zehnder interferometer, where ‘modified’ refers to 3 reflections per arm and the introduction of a deformable mirror, i.e. the MMA, in one of the arms. “Arms” refers to the non-common optical paths between the two beamsplitters and herein is labeled as left and right arms, where left and right refer to Figures 5,6,7 and 8. The VNC beam paths are described by stepping through and referencing each element in Figures 7 and 8 to the index in column two of Table-1. The color code refers to subsystem as shown in the legend of Figure 8 and delineated in column 1 of Table-1. The color-coded numbers next to each text reference in this section also refers to the elements index in column 2 of Table-1.

Source Relay Optics: The fiber passes through the tank bulkhead with a standard vacuum connector through the tank bulkhead. The light exits the fiber and expands to overfill, by $>3x$, a collimator that is encapsulated in a black baffled container that absorbs the overfill light labeled as “light trap/collimator” in Figure-7. The over fill with the aperture ensures that the wavefront and amplitude errors across the center of Gaussian beam exiting the fiber do not reduce the useful dynamic range of the MMA. At the output of the light trap is a 1 cm circular aperture [1] the aperture stop, followed by a 2” lens [2], an iris [3], a linear polarizer [4], a 2” fold flat mirror [5], and a 2” fold flat mirror [6] and a pupil lens [7]. Elements [1]-[7] collimate and condition the beam, and image the aperture stop [1] onto the MMA. The MMA is tilted with respect to incident beam, thus the aperture stop [1] is tilted such that its image on the MMA is also tilted. The iris [3] serves to mitigate

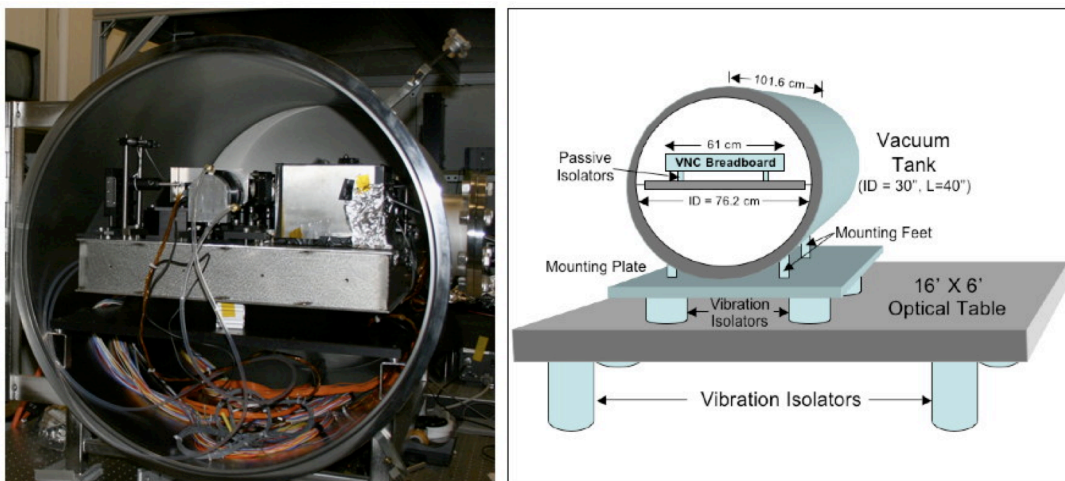


Figure-9: Left: *Previous Generation (2009) VNC in Tank*. Right: *Laboratory Configuration*

stray light that reflects off the MMA outside its active area.

Modified Mach-Zehnder (left, aka shear arm): Following the source relay optics the beam both reflects and transmits through beamsplitter-1 [8] where it transmits and reflects such that $\frac{1}{2}$ the light transmits and $\frac{1}{2}$ reflects. The reflected beam travels up and to the left in Figures 7 and 8 to transmit through the shutter [9] and linear polarizer [10] and reflects off the flat mirror [11]. The flat mirror [11] is attached to the shear mechanism. The shear mechanism is a 1-DOF linear actuated mechanism that translates [11] in a direction parallel to the input beam direction. Motion of this mirror laterally shears the beam in the left arm relative to the beam in the right arm. After reflecting from [11] the beam reflects from a flat mirror [12] then reflects from the MMA [13]. Mirrors [11][12][13] form a “W” shape and are referred to as the W-configuration. The purpose of the additional reflection, relative to a conventional Mach-Zehnder, is to minimize the angle of incidence on the MMA (20 degrees for the lab VNC). After the MMA the beam both reflects and transmits through the combining beamsplitter-2 [19] and is recombined with the beam from the right arm.

Modified Mach-Zehnder (right, aka delay line arm): The beam transmitted through beamsplitter-1 [8] transmits through a shutter [14], a linear polarizer [15] and reflects off the 3 flats mirrors [16], [17] and [18]. These three mirrors also form a “W” configuration to match the left arm and reside on a delay line carriage and translate towards or away from the incoming beam. The translation is accomplished by a two-stage mechanism consisting of a coarse mechanical 1-DOF actuator to set the path length difference, between the two arms, to zero optical path difference (OPD) to within the length of the fringe packet. The fine piezo 1-DOF actuator subsequently fine tunes the path length difference between the left and right arms to $\lambda/2 = 316.4 \text{ nm} \pm 2 \text{ nm}$ to yield a nominal path length difference, in units of radians of phase, of π -radians

The shutters, [9] and [14], in the left- and right-arms respectively, are used to block either arm or both. Shuttering both is used for detector calibration by preventing the beam from passing to the detectors; it is used to determine and store background data frames consisting of any residual stray light collected by the detectors. Shuttering of one arm, or the other, only allows the other arm to pass through to the detectors and is used to calculate the un-nulled images used to calculate the denominator of the contrast equation (equation-2) necessary to estimate contrast.

The linear polarizers [10] and [15] are initially tuned to the same linear axis as source relay polarizer [4], however, leakage from one polarization state to the other after reflecting and transmitting through the elements yields an energy imbalance between the two arms. These polarizers are tuned to balance the detector counts by interlacing observations with the shutters to ensure that the polarized light transmitted to the cameras is balanced.

Dark Focal Channel: The beams are recombined at beamsplitter-2 [19] and pass through to the dark focal channel and the bright pupil channel after reflecting off [20] and [42] respectively. The dark focal channel beam is the coherent sum of the beams from the left and right arm and reflecting from [20] and to a fold flat mirror [21] and into [22] and out of a macro zoom lens [23]. The beam exiting [23] is reflected at 90° downward (Figures 7 & 8) by fold flat [24] and passes into [25] and out [26] of a macro zoom lens and is

reflected at 90° towards the right [27]. A linear polarizer [28] minimizes cross-leakage and the fold flat [29] reflects the beam by 90° beam to the input [30] and output [31] of a macro zoom to the Lyot stop [32]. The purpose of the macro zooms at [22-23] [25-26] [30-31] is to relay the tilted image of the MMA onto the Lyot stop with unit magnification and no anamorphic distortion. The Lyot stop consists of the same hexagonal pattern of segments as the MMA (Figure-10) but with all but a circular region over each segment masked (Figure-12 right panel). This is to correct for edge glint and scatter for each segment, and to mitigate Fresnel diffraction effects (Figure-11). Following the Lyot stop the beam enters a periscope consisting of an input macro zoom [33][34], lower periscope fold flat [35], diverging lens [36], upper periscope fold flat [37] and output macro zoom [38][39]. The purpose of the periscope is the to step the beam from a beam working height of 10.16 cm (Table-1 column 6) to a working height of 18.24 cm to fold back the optical path to fit the VNC within the confines of the 36" x 24" breadboard, and to control the final image F/# such that higher than Nyquist sampling is achieved. After exiting the periscope the beam reflects 90° off a fold flat [40] and into the dark channel camera [41]. The image on this camera is an in-focus image of the 512 x 512 field of view of the camera (Figure-13 middle panel).

2.2.3 VNC Technologies

Multiple Mirror Array

The MMA is a hexagonal packed segmented MEMS deformable mirror developed under a phase-II SBIR with IRIS-AO and consists of 169 segments (Figure-10) of which 163 segments are actuated, the 6 outermost segments are not controlled and reside outside the beam footprint (Figure-12). Each segment is actuated in the 3-DOF of piston, tip, and tilt and can move over the range of 0 to >1 micron in piston, and ~ 200 arcseconds in tip and tilt. The delivered MMA has 14-bit electronics as delivered in May of 2010; 14-bits is more than adequate to reach milestone #1. Each of the segments is 606.22 microns flat-to-flat with gaps of 4 – 5 microns and each segment is ~ 4 nm rms surface error and segments are made of single crystal silicon coated with protected aluminum. The full width (from left to right) of the longest row of segments is ~ 9.2 mm. The MMA technology represents the main tall pole for the VNC laboratory demonstration at this time. Achieving high yields of quality

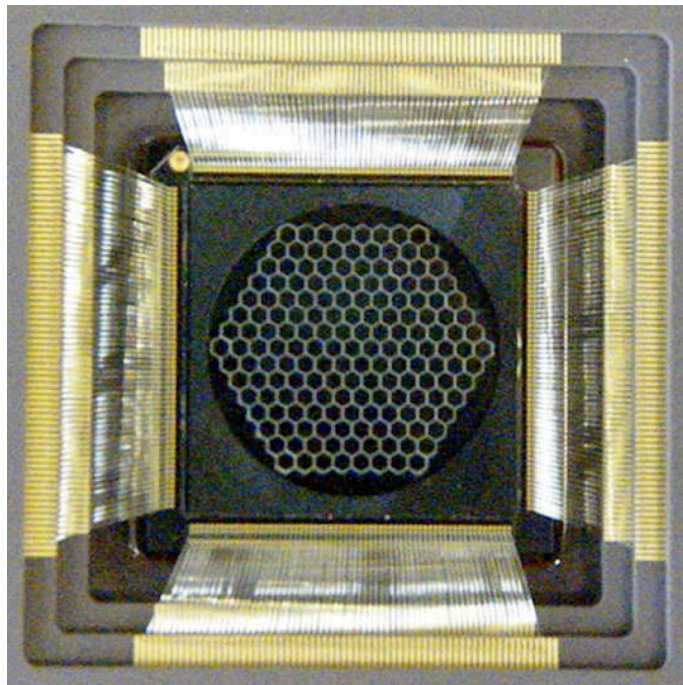


Figure-10: Multiple Mirror Array supplied by IRIS-AO 169 hex packed segments (163 actuated) MEMS based. Segments lie on a hexagonal lattice with center-to-center spacing of ~ 613 microns.

devices continues to be a challenge for MMA manufacturers. It remains for the performance of these devices, specifically stability and flatness, to be demonstrated in the laboratory environment.

Pupil Stop Mask and Lyot Stop

The pupil stop is defined to be at the MMA and is defined to be the tilted plane on which the source relay optics images the aperture stop (element-1 of Table-1). The pupil stop mask is physically the iris (element-3 Table-1), however the iris is imaged onto the MMA such that it has a sharp edge at the outer edge of MMA. The outer edge of the MMA is physically above the surface of the segments and outside the footprint of the MMA and thus this requires the iris to be in a slightly different plane than the aperture stop such that both are in focus at their respective locations on the MMA. This prevents light from causing glints and edge scatter near the edges of the MMA.

Figure-11 shows a simulated beam propagation of Fresnel diffraction versus distance for the full MMA (top row) and for a single segment of the MMA (middle and bottom rows with different scales). The small sizes of the segments (~606 μm) and segment gaps (~4 – 5 μm) cause the segments irradiance pattern to expand during propagation and all the optics after the MMA must be larger to capture the slowly expanding beam. If an element after the MMA acts as a limiting aperture then it will introduce spatial filtering that causes the segment influence functions to bleed together at the plane of the Lyot stop causing a difficult control problem unless this diffraction was well matched by a pupil mask in the shape of the MMA in the right arm of the nuller at the optic conjugate to the MMA, i.e. element-18 (Table-1). The use of the aperture stop (element-1) and iris (element-3) and oversizing the optics mitigates this problem.

The optics, prior to the Lyot stop (element-32), images the tilted MMA onto a tilted Lyot stop with unit magnification. The Lyot mask is made of blackened titanium foil, mounted in a standard optical mount, with circular holes of diameter 400 microns +/- 5 microns, with beveled edges, cut via laser ablation. The location of the center of each circular hole matches the location of each MMA segment to +/-2 microns but does not currently match the hexagonal shape of the segments. This results in a reduction in throughput in the lab VNC. The flight VNC would have higher fidelity pupil masks that would correctly match the MMA segment shapes. A custom Lyot stop was manufactured after the MMA used for the milestone was delivered and any bad MMA segments located (Figure-12) and the position and size of each MMA segmented was measured in the GSFC microscopy shop.

Mechanisms

Two lineal actuation mechanisms are used, one for overall piston differences and the other for the lateral beam shear. Each of these mechanisms is from Polytech PI and each has separate controller electronics. The piston mechanism is two-stage, coarse (10 mm range) and fine (2 nm resolution), and moves the 5 x 6 inch board (labeled 'delay line' in Figures-7) in 1-DOF. Flats elements 16, 17, and 18 (Figure-7) are all mounted on this board and move as a common unit. The piston controller is coupled to the wavefront control and it operates in closed-loop, at lower bandwidth via an integrator, to keep the mean piston motion averaged over the set of MMA segments, and averaged over the integrator weights, at zero to hold the range of piston motions on MMA segments to a region of their range.

Additionally it is used open loop during coarse acquisition of the fringes to remove larger piston biases (up to mm scale) between the two arms of the lab VNC to facilitate alignment. The 2nd mechanism is the shear mechanism and labeled in Figure-6 and is element-11 in Figures 7 and 8. It moves in 1-DOF parallel to the direction of the beam reflecting off beamsplitter-1. It effectively translates the beam in this arm of the nuller relative to the beam in the other arm and introduces lateral shear. It is used during alignment in air and subsequently retuned once in the vacuum tank, but is not moved during a data collection event, thus contrast is measured at a fixed shear setting. Additionally there are electronically controlled tip/tilt actuators on both beamsplitter-2 and on flat element-18. These are used to fine-tune the alignment after the lab VNC is moved from the staging table to the vacuum tank to ensure that the delay line motion keeps the beam in the right aligned relative to the beam in the left arm. All the other flats also have tip/tilt thumbscrew type actuators that are set outside the vacuum tank and are not moved once inside the tank. The MMA is mounted in a Ziff socket mounted to PC

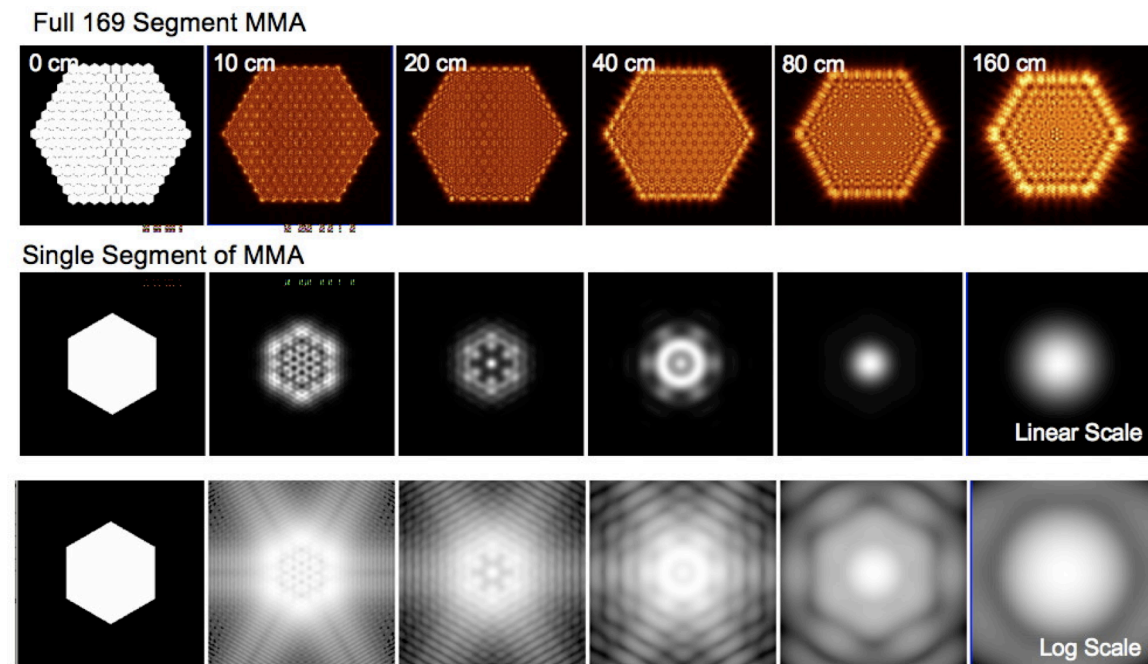


Figure-11: Top Row: *Fresnel Diffraction from MMA at distances 0, 10, 20, 40, 80, and 160 cm.* Middle and Bottom Rows: *Fresnel Diffraction of a Single MMA Segment at same distances on linear and log scales respectively.*

board. The PC board is mounted via screws to a stiff aluminum backplane board that in turn is mounted to a custom tip/tilt stage with stiff springs used in tension. It has a high natural frequency and the center of the tip/tilt is approximately at the center of the MMA surface. There are two electronic shutters (Figures-7 and 8) and listed in Table-1 as elements 9 & 14. There is one shutter per nuller arm, that operate as very low bandwidth choppers during sensing and control to measure background counts on the detector and measure the relative intensity in each arm of the interferometer. These are operated every 2.5 seconds in the tank and are binary devices, i.e. open or closed, and used for assessing and compensating for source brightness drift and temperature drifts of the detectors.

Detectors

The bright detector is a CMOS high frame rate camera and the dark output camera is a low-light high linearity EMCCD camera (Wen 2006). These cameras are framed at their own individual rates. The bright pupil channel uses a low cost Pixelink CMOS camera that can display on a monitor at video rates and save frames to disk. The dark focal channel uses a TEC cooled EMCCD camera (-70C) with gain set to 1 ADU per 3 photoelectrons.

2.3. Error Budgeting & Traceability of Lab Demonstration to EPIC

This section describes the basis for our lab error budgeting and succinctly discusses the top-level EPIC error budget and the lab vacuum VNC error budget and shows the important differences between the lab VNC and that which is required for flight.

2.3.1 Basis of Error Budgeting Formalism

The noise free image irradiances in the single nuller's bright and dark focal planes are given by:

$$\begin{cases} I_B(\theta) = \frac{1}{2}I_1PSF_0(\theta) + \frac{1}{2}I_2PSF_\phi(\theta) + \sqrt{I_1I_2} \operatorname{Re}\{ASF_0(\theta)ASF_\phi^*(\theta)\} \\ I_D(\theta) = \frac{1}{2}I_1PSF_0(\theta) + \frac{1}{2}I_2PSF_\phi(\theta) - \sqrt{I_1I_2} \operatorname{Re}\{ASF_0(\theta)ASF_\phi^*(\theta)\} \end{cases} \quad (5)$$

where $I_B(\theta)$ and $I_D(\theta)$ represent the bright and dark channel output images, θ is the angular variable representing the focal plane projected on the sky, and where $I_1 + I_2 = I_{STAR}$. I_{STAR} is the integral over sky angle of the stellar flux collected by the telescope and for the lab VNC is the spatial integral of the irradiance in the pupil masked region prior to it impinging on beamsplitter-1. I_1 and I_2 are the beamsplitter reflected and transmitted fluxes. PSF represents the optical point spread function of the stopped pupil, including the beam shear, and the subscript '0' represents the unaberrated PSF and the subscript 'ϕ' represents the aberrated (phase and/or amplitude) PSF. Both PSFs are normalized such that their integrals over $d\theta$ are unity. ASF is the complex amplitude spread function such that $PSF = |ASF|^2$. It is straightforward to show that $I_B(\theta) + I_D(\theta) = I_1PSF_0(\theta) + I_2PSF_\phi(\theta)$ and thus the integral of this sum is $I_{STAR} = I_1 + I_2$. The phase and amplitude aberrations can be ascribed to one arm or the other of the interferometer without loss of generality since it is only differences that matter.

Expanding the dark channel equation (2nd equation in (5)) using the small angle approximation for the phase error, i.e. $e^{i\phi} \approx 1 + i\phi$, results in the relation that

$$C = \frac{I_{PLANET}}{I_{STAR}} \approx \left(\frac{\pi W_0}{\lambda} \right)^2 PSF_0(\theta - \theta_{PLANET}) \text{ where } \theta_{PLANET} \text{ is the location of the planet and}$$

W_0 is the wavefront error amplitude at one given spatial frequency. If the mean wavefront error is zero (equivalent to piston difference between nuller arms being zero) then the average contrast is $\langle C \rangle \approx \left(\frac{\pi W_0}{\lambda} \right)^2$. The brightness of speckles is exponentially distributed such its mean is equal to the standard deviation of its intensity, and since we desire to set the requirements for the VNC based on high confidence statistics we require $\langle C \rangle + 3\sigma_{\langle C \rangle} = 4\langle C \rangle \leq C_{FLIGHT}$ where C_{FLIGHT} is the flight requirement limit. This ensures that the flight contrast limit will be met better than 99% of the time. Solving the contrast equation for a single spatial frequency wavefront term gives $W_0 \approx \frac{\lambda}{2\pi} \sqrt{\langle C \rangle}$ per spatial frequency. The rms of this term is $W_{RMS} \approx \frac{1}{\sqrt{2}} \frac{\lambda}{\pi} \sqrt{\langle C \rangle}$ per spatial frequency.

For the lab VNC operating at $C=10^{-8}$ at $\lambda=633$ nm requires $W_{RMS} \approx 0.014$ nm rms per spatial frequency. The overall rms wavefront error (WFE) is obtained by integrating W_{RMS}^2 over all spatial frequencies of interest. Spatial frequencies of interest are limited for the lab VNC to what is controllable by the MMA. The MMA has 169 segments of which 158 are active and each has 3 control degrees of freedom (DOF) for 474 control DOF in all. The number of control DOF across the diameter of the beam is given by $\sqrt{\frac{\pi}{4} DOF}$.

Using W_{RMS}^2 as the circular PSD, with random phase (white noise assumption) and integrating from 0 to $f_{HI}=8$ cpa, i.e. the Nyquist of the 2D spatial frequencies defined by the outer edge of dark hole mask (Figure 14 upper left) gives $\sigma_{WFE} = \lambda \sqrt{\frac{2}{\pi}} f_{HI} \sqrt{\langle C \rangle}$ for the rms WFE. To achieve contrast of 10^{-8} at $\lambda=633$ nm requires $\sigma_{WFE} \leq 0.202$ nm rms WFE where this is the rms difference of the wavefront error between the two arms of the nuller, if all other error sources are considered negligible. However, this is not the case since there are other terms that include intensity variation due to coating imperfections, differential polarization, and finite spectral bandpass.

The lab VNC uses sampling at a plate scale $>7x$ higher than Nyquist sampling. This oversample does not change the wavefront error requirement to achieve contrast, however, it does allow more photons per speckle without saturating the residual bright image core; this has the net effect of higher signal-to-noise sensing and control.

Intensity variations, differential polarization and finite spectral bandpass can all be estimated by a similar expansion of equation (5) and results in the following approximations for the bright and dark channel irradiance:

$$\begin{cases} I_B(\theta) \approx \frac{1}{1 + \frac{\pi^4}{8}\theta^3} \left[1 - \left[\pi^2 \left(\frac{\sigma_w}{\lambda} \right)^2 + \frac{\sigma_I^2}{16} + \frac{\sigma_\psi^2}{4} + \frac{\pi^2}{48} \left(\frac{\Delta\lambda}{\lambda_0} \right)^2 \right] \right] \\ I_D(\theta) \approx \frac{1}{1 + \frac{\pi^4}{8}\theta^3} \left[\pi^2 \left(\frac{\sigma_w}{\lambda} \right)^2 + \frac{\sigma_I^2}{16} + \frac{\sigma_\psi^2}{4} + \frac{\pi^2}{48} \left(\frac{\Delta\lambda}{\lambda_0} \right)^2 \right] \end{cases} \quad (6)$$

In equation (6), θ is the focal plane location in units of λ/D , σ_I^2 is the variance of the intensity in fractional units, σ_ψ^2 is the variance of the differential polarization rotation in radians of polarization vector rotation, $\Delta\lambda$ and λ_0 are spectral bandpass and central wavelength respectively. The 2nd equation in Equation (6) can be converted into a generalized form by defining $\sigma_{E:I} \equiv \frac{\lambda}{4\pi} \sigma_I$, $\sigma_{E:\psi} \equiv \frac{\lambda}{2\pi} \sigma_\psi$ and $\sigma_{E:\Delta\lambda} \equiv \Delta\lambda/4\sqrt{3}$ to yield a form where all the contributors are in equivalent units of nanometers rms:

$$I_D(\theta) \approx \frac{1}{1 + \frac{\pi^4}{8}\theta^3} \left(\frac{\pi}{\lambda} \right)^2 \left[\sigma_w^2 + \sigma_{E:I}^2 + \sigma_{E:\psi}^2 + \sigma_{E:\Delta\lambda}^2 \right] \quad (7)$$

Equation (6) is incorporated in the error budget described in section 2.3.2. It is worthwhile to note that dark channel irradiance is proportional to the variances of the individual contributors and thus lends itself to a straightforward recipe for error budgeting by summing the variances for each optic for each contributor.

This ensures that the mean contrast plus its 3-sigma is at or below the Milestone #1 contrast of 10^{-8} to a confidence of better than 99% and forms the basis for the lab VNC error budgeting.

2.3.2 Description of Error Budgets

Table-2 gives a high level description of the roll-up of the various contributors to the EPIC error budget to meet contrasts of 10^{-8} (disks), 10^{-9} (jovians), and 10^{-10} (Earths) at a $2.8 \lambda/D$ IWA corresponding to 175 milli-arcseconds (mas) at $\lambda=500$ nm for a 1.65 m diameter telescope. Since EPIC requires a dual nuller, each of which operates independently at $2 \lambda/D$, milestone #1 addresses a single nuller contrast of 10^{-8} at $2 \lambda/D$ where $\lambda=633$ nm and D is the beam diameter of 1 cm giving an IWA on the testbed of 13 arcseconds. The “residual WFE” is the static allowable rms wavefront error during science observation, while “WFE drift per control step” is the allowable drift during closed-loop including sensing and controller errors. No time or control bandwidth need be included since if the control is slow then the drift is the allowable random error during successive control steps. The EPIC contributor of beam walk per control step is irrelevant for the lab VNC since there is no pointing induced beam walk. The values for “LOS jitter” and “Beam Walk per WFC step” are allocations that were used in the EPIC models (Clampin 2009). Note that there are numerous other allocations that result in the same contrast. The optimal would be based on technology cost and risk but that parameter

trade space has only been explored in a limited sense. The polarization error is mitigated for Milestone #1 by using a polarizer that only allows the transverse electric field component to be incident on the beam splitter and an analyzer after the 2nd beamsplitter only allows this same polarization state to reach the focal plane. Pointing precision in the lab shows up as pointing jitter between the optics and is just scaled by the ratios of the flight to lab IWA. For Milestone #1 no attempt is made at amplitude control and thus the amplitude difference between the two-nuller arms is maintained by coating specifications on the optics.

Table-2: EPIC's WFE and Stability Error Budget

EPIC Contributor @ 125 mas	Units	Disks	Jovians	Earths
		10 ⁸	10 ⁹	10 ¹⁰
Residual WFE	nm RMS WFE	0.038	0.012	0.004
WFE drift per control step	nm RMS WFE	0.070	0.022	0.007
RMS Reflectivity error	%	0.158	0.050	0.016
Polarization Error	degrees	0.032	0.010	0.003
Pointing precision (LOS jitter)	mas (3 σ)	7.310	4.100	2.245
Beam Walk per WF control step	mas (3 σ)	7.310	4.100	2.245
Contrast at 125 mas (2 λ/D) =		1.0E-08	1.0E-09	1.0E-10

Table-3 shows the error budget for the lab VNC for each optical surface with three contributors on each surface: (i) *Intensity*, (ii) *WFE*, and (iii) *Diff Pol*, each of which are defined and described below. This error budget is for the dark output arm of the lab VNC and its format is such that it follows the light path through the lab VNC. It starts in the 1st column to the left for the Source Module and Flats 1 and 2 and continues to the 2nd and 3rd columns which are the non-common path interferometric optics comprising the nulling interferometer. It subsequently continues to the common path optics following the interferometric section of the nuller and rolls up the uncorrected errors in the box labeled 'Uncorrected Errors' to the upper right.

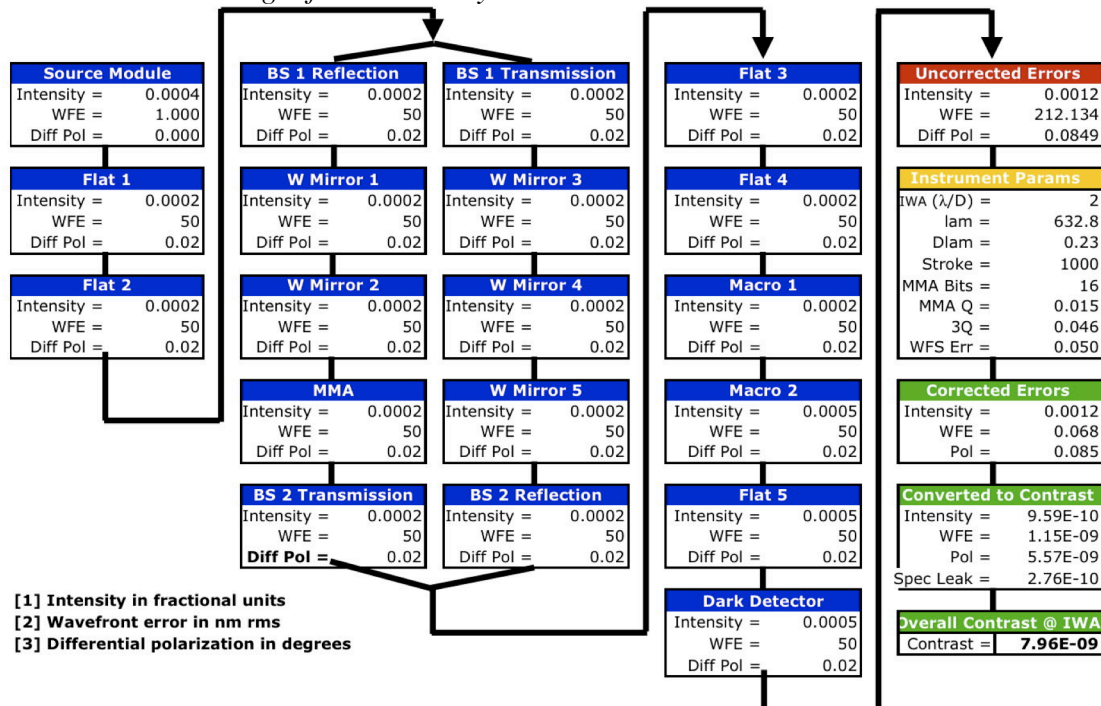
The relevant instrument parameters are in the box labeled in yellow and consist of the IWA in units of λ/D , the central wavelength in nm, the bandpass in nm, the stroke of each MMA segment in nm, the number of bits in the MMA control electronics, the quantization 'Q' of MMA stroke, i.e. stroke per bit, and the wavefront sensing error in nm rms. The difference between 'Uncorrected Errors' and 'Corrected Errors' (in red) are that the wavefront error is reduced. It should be noted that inner working angle for a single nuller arm is 2 λ/D , while it is 2.8 λ/D for the complete VNC design with two nuller arms.

Intensity is the relative standard deviation of reflectivity over the region of the beam footprint on that optic. All the flat optics, except for the DM and its conjugate, are Semrock flats with <2% variability in coating thickness. Using a thin film model and assuming a 150 nm thick coating gives a very small intensity variation of the transverse electric component of $\sim 3 \times 10^{-6}$ (1-sigma) across the diameter of the beam. We adopted a conservative approach and used $\sigma_{\text{Intensity}} = 0.0002$ on all the flats. The intensity variation in the source module is based on a sheared truncated Gaussian beam model that yields 0.0004. Flats 1 and 2 are the two flats following the source module and intensity variations occur in common mode and hence do not matter. Flats 3, 4, 5 and Macro 1 and 2 intensity variations also do not matter interferometrically since they appear in common

mode, i.e. in the recombined beam and hence do not contribute to the null depth. However they, along with Flats 1 and 2 contribute to the size and brightness of a speckle since they reduce the brightness of a given speckle by spreading it out. The MMA is coated with protected aluminum (Al + SiO₂) as its counterpart flat (W Mirror-5) in the other arm of the interferometer. Both the MMA and its counterpart flat have a pupil stop in front of them to ensure that the diffraction in each arm is the same. The pupil stop is a mask with holes centered on each of the MMA segments.

WFE is the rms wavefront error of each given optic and is nominally 50 nm rms ($\lambda/10$ @ $\lambda = 500$ nm) for each except the source module (assumed to be 1 nm). The 50 nm rms is from the vendor quote for the optics over their clear aperture, however, these optics are higher quality when measured over the smaller beam footprint of the lab VNC. Two of the Semrock flats were $\sim\lambda/100$ rms WFE when tested on our lab Zygo interferometer. Flats 1, 2, 3, 4, and Macros 1 and 2 and Flat 5 matter little since these occur as common path optics.

Table-3: Error Budget for laboratory nuller.



Diff Pol is the rms differential polarization in units of degrees. It is the cross leakage of the transverse electric polarization state on each optic due to local coating and tilts on the optic and leakage in the coatings. The effect of the polarization cross leakage is to induce a loss of contrast due to the cross-leaked polarization term adding incoherently to the transverse polarization term. A 2nd polarizer, with its polarizer axis aligned to the 1st polarizer, reduces cross-leakage on the dark output beam prior to the detector.

If each of 4-terms are converted to equivalent rms wavefront error per the form shown in Equation (7) then the root sum square (RSS) of the 4-terms (WFE, intensity error, differential polarization, and spectral leakage) yield 0.200 nm equivalent rms WFE.

2.3.3 VNC Point Spread Function and Plate Scale

Point Spread Function

The VNC point spread function (PSF) is determined by evaluating the diffraction integral that describes the propagation from the pupil (plane of the aperture) to the focal plane. The diffraction integral is given by:

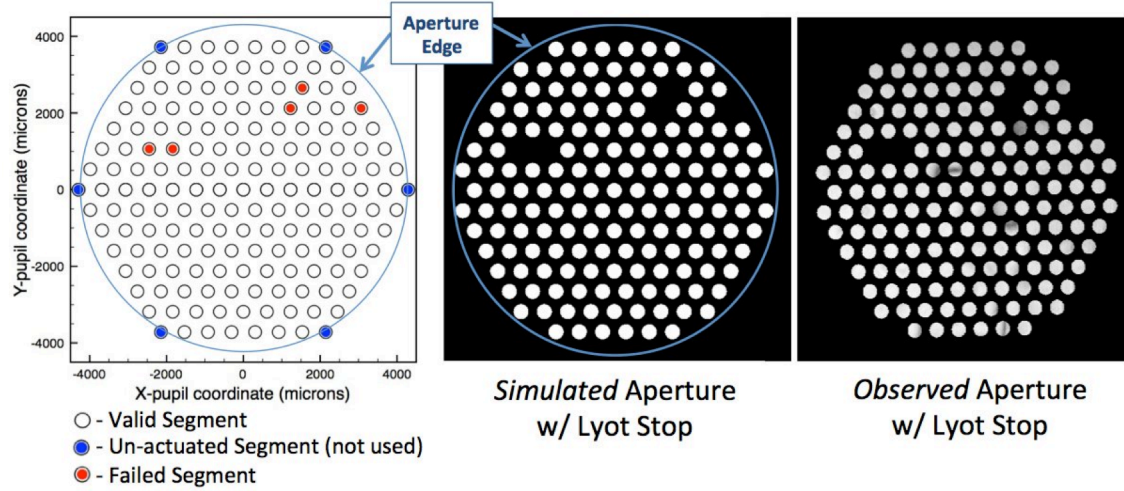


Figure-12: *Simulated and Observed VNC Aperture*

Left: Map of valid segments, *Middle:* Simulated aperture of valid segments, edge of Lyot stop is shown as blue circle and defines “D”, i.e. the diameter = 8582 microns, *Right:* Observed VNC aperture after Lyot stop. Note the pitch (center-to-center spacing) of each segment is 613 microns and the Lyot stop hole on each segment is 400 microns diameter.

$$E(\theta_x, \theta_y) = \frac{1}{\lambda} \sqrt{\frac{n_T}{\Delta A}} \iint A(x, y) e^{i\phi(x, y)} e^{-i2\pi\left(\frac{\theta_x}{\lambda}x + \frac{\theta_y}{\lambda}y\right)} dx dy \quad (8)$$

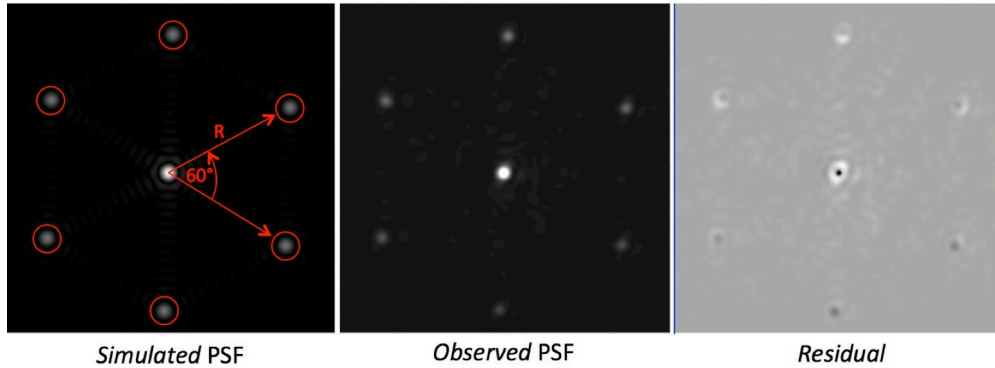


Figure-13: *Simulated, Observed and Residual PSFs for Plate Scale Fitting*

Table-4 – VNC Image Plate Scale

index of peak	Location of Peak		Peaks relative to center		Radius	Angle
	x	y	x - <x>	y - <y>	r	(degrees)
1	446	345	188.67	97.50	212.37	27.33
2	434	142	176.67	-105.50	205.77	-30.84
3	250	37	-7.33	-210.50	210.63	88.00
4	71	150	-186.33	-97.50	210.30	27.62
5	78	355	-179.33	107.50	209.09	-30.94
6	265	456	7.67	208.50	208.64	87.89
<x>, <y> =	257.33	247.50		<r> =	209.47	pixels
				σ =	2.23	pixels
				StdErr =	0.91	pixels
M (rings) =	7			fit plate sca	0.06778	λ/D per pix
				Peaks @	14.19714	λ/D radius
# Segmts =	169			+stderr =	0.06748	
pitch: d =	613	microns		-stderr =	0.06807	
aper: D =	8582	microns		delta =	-0.00029	
Hole: H =	400	microns		delta =	0.00030	
D/d =	14			StdErr =	0.00030	
2D/√3d =	16.16581	λ/D				
			Plate scale:	0.06778 ±0.0003		λ/D per pix

The total area of the aperture is ΔA , λ is the wavelength, n_T the total number of photons collected by the aperture per wavelength, and $A(x,y)$ is the $[0,1]$ aperture function (Figure-12 center) and is unity where light passes and 0 where it does not. The phase errors, $\phi(x,y)$, are given by the product $\frac{2\pi}{\lambda}W(x,y)$ where $W(x,y)$ is the wavefront error and (x,y) are the coordinates in the plane of the aperture. Equation (8) is normalized such that $\iint |E(\theta_x, \theta_y)|^2 d\theta_x d\theta_y = n_T$ when the integral is taken over all focal plane angles (θ_x, θ_y) and it is the total number of photons collected by the aperture. The PSF for a segmented aperture, with all the segments, is given by (see Yaitskova et al. [12]):

$$PSF(\vec{\theta}) = \frac{4n_T J_1^2\left(\frac{\pi h}{D}|\vec{\theta}|\right)}{N^2 \left(\frac{\pi h}{D}|\vec{\theta}|\right)^2 \sin^2\left(\frac{\pi d}{D}\theta_x\right)} \left\{ \begin{array}{l} \left[\frac{\sin\left(\frac{\pi d}{2D}((3M+1)\theta_x + (M+1)\sqrt{3}\theta_y)\right)}{\sin\left(\frac{\pi d}{2D}(\theta_x - \sqrt{3}\theta_y)\right)} \frac{\sin\left(M\frac{\pi d}{2D}(\theta_x - \sqrt{3}\theta_y)\right)}{\sin\left(\frac{\pi d}{2D}(\theta_x - \sqrt{3}\theta_y)\right)} \right]^2 \\ + \left[\frac{\sin\left(\frac{\pi d}{2D}((3M+2)\theta_x - M\sqrt{3}\theta_y)\right)}{\sin\left(\frac{\pi d}{2D}(\theta_x + \sqrt{3}\theta_y)\right)} \frac{\sin\left((M+1)\frac{\pi d}{2D}(\theta_x + \sqrt{3}\theta_y)\right)}{\sin\left(\frac{\pi d}{2D}(\theta_x + \sqrt{3}\theta_y)\right)} \right]^2 \end{array} \right\} \quad (9)$$

Where D , d , and h are respectively the diameter of the full aperture (blue circle in Figure-12), pitch of DM, and diameter of the circular mask on each segment, and (θ_x, θ_y) is units of λ/D . The zeros of the denominator of equation (9) give the focal plane location of the peaks as:

$$\begin{cases} \theta_x = n \frac{D}{d} \\ \theta_y = \pm \frac{2m-n}{\sqrt{3}} \frac{D}{d} \end{cases} \rightarrow |\theta| = \frac{2}{\sqrt{3}} \frac{D}{d} \sqrt{n^2 + m^2 - mn} \quad (10)$$

The peaks form a hexagonally symmetric grid pattern of peaks, diminishing in brightness with increasing radial distance. The VNC, when operating in its nominal condition, shows only the central peak and the surrounding closest 6 peaks due to the limited field of view subtended by 512 x 512 camera. The theoretical six focal plane locations of the peaks, in units of λ/D , surrounding the center are at:

$$(\theta_x, \theta_y) = \frac{D}{d} \left\{ \left(1, \frac{\pm 1}{\sqrt{3}} \right), \left(0, \frac{\pm 2}{\sqrt{3}} \right), \left(-1, \frac{\pm 1}{\sqrt{3}} \right) \right\} \quad (11)$$

These span 60-degree angles and are all at the same radius from the central peak. These are the theoretical peak locations for a fully populated MMA, i.e. with all segments. However, the VNC's MMA is not fully populated and the missing segments results in shifts of the peak locations.

Plate Scale

The plate scale for the VNC is determined from a two-step process using the observed lab PSFs. In the first step we visually estimate the (i, j) pixel indices (Table-4, columns 2 and 3) of the 6 peaks in the image and map them to λ/D units via equation (11) to give a starting point for the nonlinear fitting in the second step. The second step minimizes the rms difference between an observed and simulated PSF by varying the (x, y) shift, rotation angle, and plate scale of the simulated PSF, but only over the masked regions (red circles in Figure-12 left), until the simulated PSF matches the observed PSF in a minimal rms sense. The VNCs mirror array differs from a filled hexagonal array in that the 6 outer segments are not actuated (left panel of Figure-12 closed blue circles) and 5 other segments are failed (left Figure-12 closed red circles); these 11 segments are masked out by the VNCs Lyot stop and therefore do not contribute to the PSF. Figure-12 (left) shows the map of the valid segments; for the VNCs MMA there are 7 rings of segments plus the central segment giving a total of $N=3M(M+1)+1=169$ where $M=7$ is the number of rings. The remaining 158 valid segments are shown as open circles in the left panel of Figure-12.

Figure-13 shows the resulting simulated and observed focal plane PSFs with the 6 peaks shown within the red circles and the distance and angles labeled. The nonlinear fit results in the results of $(dx, dy)=(-2.2, -8.8)$, rotation = 1.808 degrees (clockwise) and a plate scale of **$0.06778 \pm 0.0003 \lambda/D \approx \lambda/14.754D$** per pixel, i.e. 7.38x Nyquist sampled. It is this plate scale that we use for the VNC. The highly sampled images arising from this plate scale tend to spread the light over larger areas thereby allowing more photons per speckle for higher signal-to-noise ratio sensing and control, and for mitigating detector charge leakage effects from the brighter core of the image.

2.3.4 Design of VNC Diagonal Wavefront Control Modes

The VNC uses a hexagonally packed deformable mirror called the MMA. Controlling each of the MMA's hexagonal segments in piston, tip and tilt by 3 voltage driven actuators, in closed-loop, allows the VNC to increase the contrast within the dark hole. Iterative closed-loop control allows deeper contrast to be obtained, and held. Each actuator voltage is controlled in the software. Each of the MMA segments piston, tip and tilt influence functions are orthogonal in that motion of one doesn't influence the others. However, since we desire a

dark hole in a specific focal plane region (Figure-14) it is more efficient to couple linear combinations of actuators together into a set of control modes. This results in a smaller set of control modes enabling a trade between higher control bandwidth and instrument level temporal stability. The set depends on the size and location of the dark-hole region and on the sensing noise floor due to vibration and camera noise. In this section we discuss the procedure we employed for the design of the set of control modes used to achieve the milestone.

Design Procedure:

1. We first numerically generated a set of orthogonal basis column vectors, \mathbf{B}_j . Each basis vector represents either piston, tip, or tilt in the pupil (plane of the MMA), and where the number of basis vectors is equal to the number of degrees of freedom, $N_{DOF} = 3 \times N_{Seg} = 474$, where $N_{Seg} = 158$ is the total

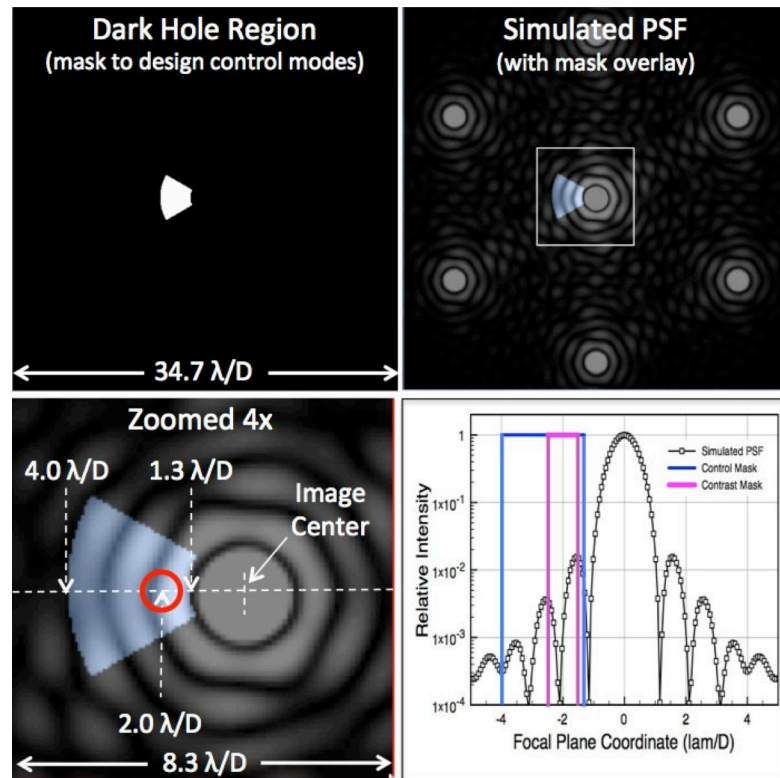


Figure-14: Dark Hole Region, Location and Size. Top Left – Focal plane mask defining region (white) to optimize control modes over. Top Right – Dark hole region as overlay on simulated PSF. Lower Left - Control modes are designed to achieve the milestone within the region shown in blue (4x scale than upper right). Red circle shows region of diameter $1 \lambda/D$, centered at $2 \lambda/D$ over which the contrast for milestone is calculated. Lower Right – Plot from left-to-right along dashed line on lower left panel that shows the control mask extending from -4.0 to $-1.3 \lambda/D$.

number of valid segments; thus $j = 1, \dots, N_{DOF}$. Each basis vector is a column vector consisting of a 2D pupil image of size $N_s = 512 \times 512$ discrete samples lexicographically reordered into a 1D column vector of length 512^2 (Murphy 2001). Each basis vector represents pure piston, tip or tilt of a single MMA segment and each is normalized such that it is orthonormal in the sense that $\mathbf{B}_j \cdot \mathbf{B}_k = \{1 \text{ for } k = j, 0 \text{ for } k \neq j\}$. The set of basis vectors are combined, column wise, to construct the influence matrix $\mathbf{R} = [\mathbf{B}_1, \mathbf{B}_2, \dots, \mathbf{B}_{NDOF}]$ where each influence matrix column vector is the j -th basis vector, and where each basis vector is mapped to the voltage of a single MMA segments controllable DOF. Since the influence vectors (columns) are orthonormal the matrix $\mathbf{R}^T \mathbf{R}$ is diagonal, of size 474×474 , with zero off-diagonals elements and unity diagonal elements. Linear combinations of these basis vectors span all commandable motions of the MMA. This basis, however, is not optimal for control within the region of the dark hole.

2. The dark hole region is then incorporated by numerically propagating each basis vector through the simulated VNC via the small angle approximated equation given by $\tilde{\mathbf{P}}_j = -\frac{i}{2} k \mathbf{H} \mathbf{B}_j$ where \mathbf{H} is the discrete Fourier transform operator such that its output has the same plate scale (sampling) as the lab VNC (section 2.3.3). The dark hole region is imposed by averaging the dot products of the focal plane complex fields over the region of the dark hole resulting in a complex self-adjoint matrix for the jk basis vectors given by:

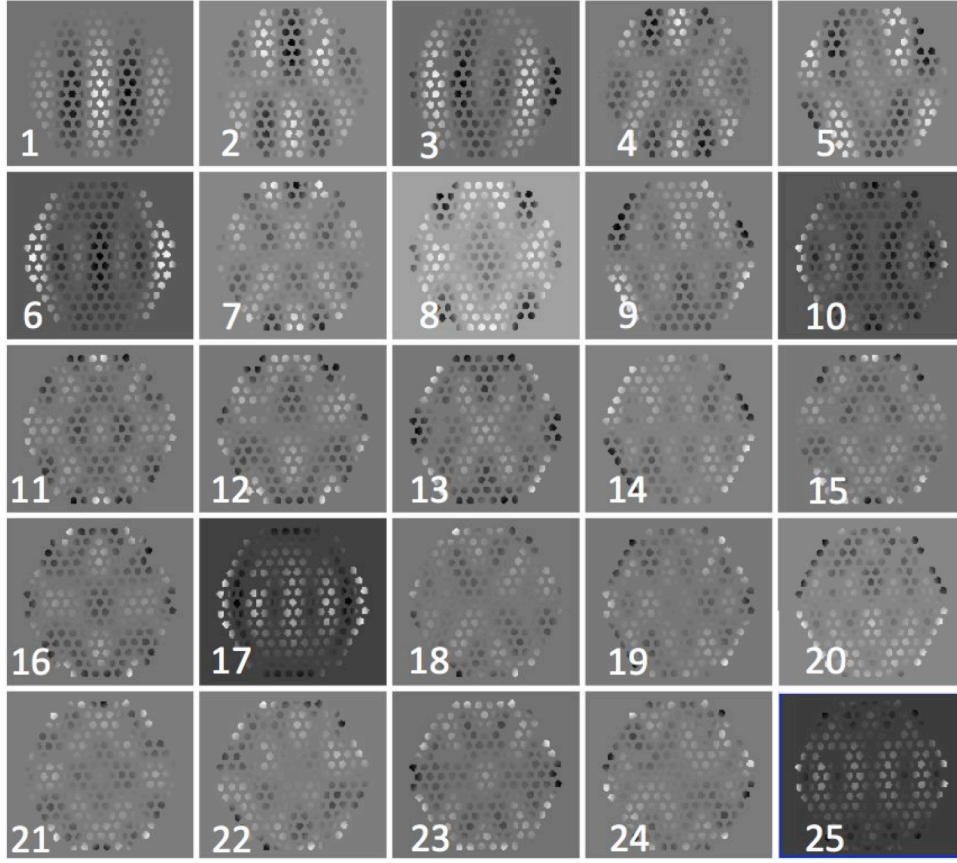


Figure-15: First 25 MMA Diagonal Wavefront Control Modes. Each mode consists of a weighted linear combination of segment piston, tip, tilt on valid segments - 474 modes in all of which the first 25 are shown.

$$[\mathbf{J}]_{jk} = \frac{1}{N_H} \sum_{m=1}^{N_H} M_m [\tilde{\mathbf{P}}_j^\dagger \cdot \tilde{\mathbf{P}}_k]_m \quad (1)$$

The mask representing the dark hole is given by M_m for $m \in [1, N_H]$ where N_H is the total number of samples within the dark hole, and since the focal plane fields are sampled at the VNC sampling it implicitly incorporates the sampling as part of the design procedure. The mask is unity within the dark hole and zero outside it.

3. This matrix \mathbf{J} is given by the conjugate dot product of the mask weighted focal plane fields averaged over the region of mask and \mathbf{J} is a square ($N_{DOF} \times N_{DOF}$) complex self-adjoint (equal to its transpose conjugate) with real eigenvalues. The diagonal elements are real since they are the modulus squared, but \mathbf{J} is not in general diagonal. The non-zero off-diagonal elements imply that the basis vectors have crosstalk. We eliminate the crosstalk by diagonalizing \mathbf{J} , using singular value decomposition (SVD) (Golub, 1996), to find the unitary transformation such that $\mathbf{U}^\dagger \mathbf{J} \mathbf{U}$ is diagonal and to re-order the resultant SVD eigenvalues such that the first basis vector (eigenvector) gives the largest change within the region of the dark hole; successive basis

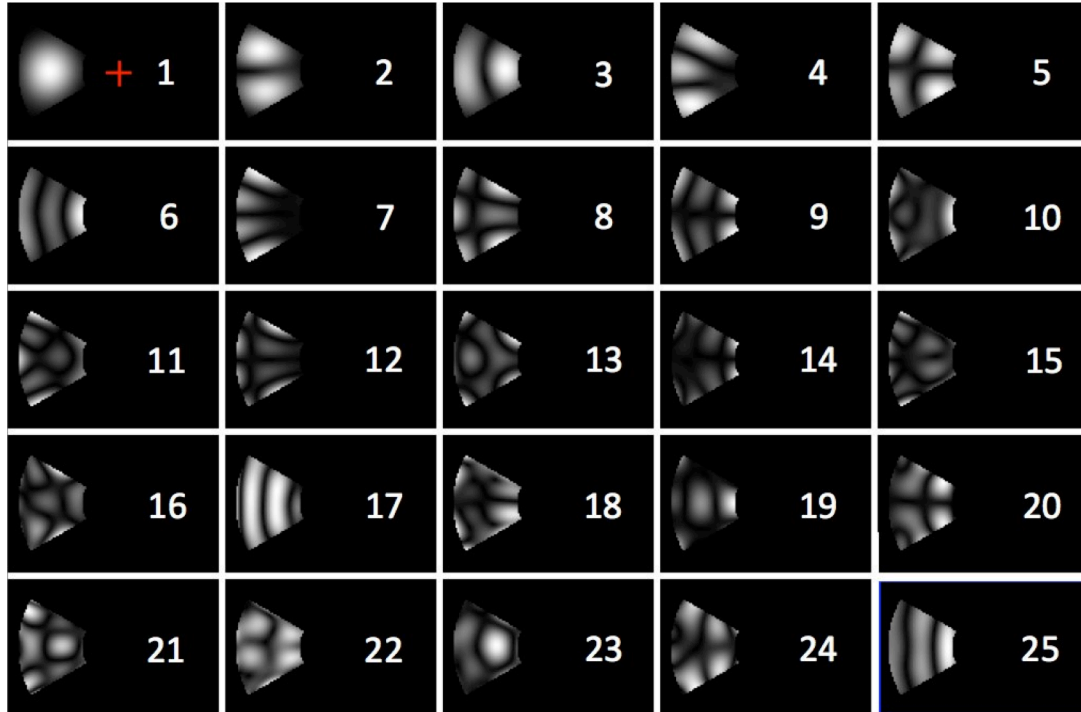


Figure-16: First 25 Control Modes in Focal Plane. Each shown as modulus squared of field for each focal plane control mode. The small asymmetries are due to the effect of the 5 failed MMA segments during the design of the control modes.

vectors giving progressively smaller changes. This results in a set of complex focal plane fields, one field per basis vector.

4. Each of the diagonal focal plane fields are separately back propagated to the pupil plane of the MMA via inverse Fourier transforms and are renormalized such that the modulus squared over the region of the valid segments is unity. This new set of basis vectors (Figure-15) are orthonormal and form a unique set of linear combinations of segment piston, tip, and tilt that gives the largest change per mode over the region of the dark hole (Figure-16). These are what we refer to as the “modes” or “control modes” herein and the first 25 are shown in Figure-15 (pupil plane)

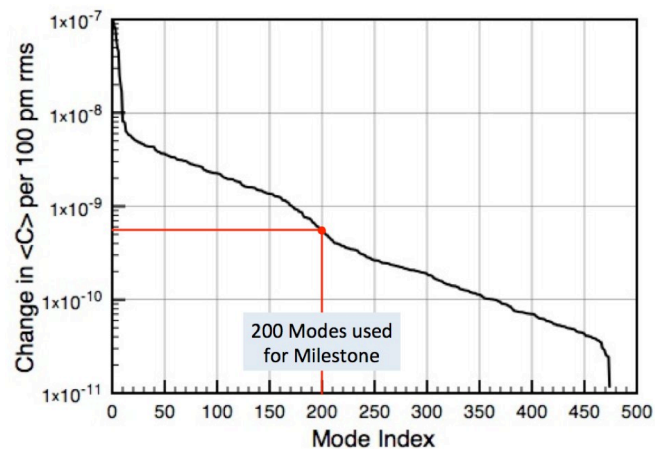


Figure-17: Modal Control Sensitivity. Mean contrast change per 100 picometers (pm) rms of control modes versus mode index. Sorted sensitivities are plotted in descending order to select minimal set of modes – 200 modes used for milestone with mode 200 giving a sensitivity of $\sim 5.5 \times 10^{-10}$ contrast change/100 pm. Fewer control modes implies faster control.

and Figure-16 (focal plane).

2.3.5 Validation and OSCAR Modeling

A component of this effort is to validate the error budgeting against laboratory data and to understand and rectify differences. Validation within the scope of this effort is limited to demonstrating that the optical and control requirements set by analysis and modeling, yields the expected results for contrast at the IWA. The error budget formalism itself is based on approximations that make the theory tractable and lend itself to development of parametric error budgets within the confines of spreadsheets. The question that remains is whether these approximations are accurate enough and capture all the physics. It is likely that some portion of the error budgeting will require more comprehensive models beyond the scope of the current effort. Detailed modeling is a separate effort and past efforts for the VNC have used the Optical Systems Characterization and Analysis Research (OSCAR) paradigm. OSCAR is a suite of software, developed by R. Lyon, developed in “C” and/or “C++” with a message passing interface (MPI) for modeling of optical systems; MPI is for parallel processing for those components of a problem which require it. OSCAR contains raytrace and multiple beam propagators to step an optical field surface to surface to the detector, and it models the effects of wavefront errors, surface deformations and alignments, metallic and dielectric coatings, polarization, jitter etc.

OSCAR is the Optical Systems Characterization and Analysis Research software for modeling and beam propagation through telescopes, interferometers, coronagraphs and spectrometers. OSCAR began life at Perkin-Elmer in the late 1980’s to model Hubble point spread functions (PSF) as seen through the HST Faint Object Camera (FOC), Wide Field/Planetary Camera (WF/PC), and the response of the Fine Guidance Sensors (FGS) by modeling beam propagation through the Koester’s prism interferometer. The raytrace components of OSCAR were validated at Perkin-Elmer, using their in-house MEXP software, by tracing rays through HST and to the instruments focal in both OSCAR and MEXP and validating that both the ray intercepts and ray angles at each surface agree for the two packages to 6 significant figures. In the late 1980’s OSCAR was used to model diffractively the images of unresolved stellar sources through various optical filters with the effects of scatter, sampling, and detector noise. The simulated images were used as inputs to test our pre-launch HST phase retrieval algorithm (Grey and Lyon, 1989). At that time OSCAR was referred to as “Pmod” for Phase modeling. It primarily included raytracing, and pupil-to-pupil and pupil-to-focal plane beam propagation modeling. OSCAR was subsequently used on the AFRL Mid-Course Space Experiment (MSX) to optically model the point response function (PRF) for the SPIRIT-III radiometer. This work was validated against PSFs and MTFs measured during thermal vacuum testing by USU’s Space Dynamics Lab (SDL). The results were documented in (Lyon, 1994). The OSCAR simulated PRF’s were subsequently used to design and develop the software for processing of the MSX data for image construction and later deconvolution (Lyon, 1994).

Starting in 1994 both OSCAR’s fidelity and speed were increased. OSCAR was expanded to include not just Zernike polynomials on each surface but also other bases including Fourier and Fourier-Polar. HST/FOC images spanning the spectral range 275 – 889 nm were simultaneously phase retrieved with an algorithm based on OSCAR as the

propagator to determine the mid- and higher-spatial frequency structure on the HST mirrors and the these mirror maps were built into OSCAR. Additionally OSCAR was parallelized to execute on a MasPar MP-II array processor and later in C/MPI to execute on Beowulf clusters and other parallel computers. OSCAR was further validated using observed pre- and post-COSTAR corrected HST images (Lyon, et. al, 1997) and the resultant higher fidelity version of OSCAR was used to synthesize PSFs for HST scientific work on symbiotic jet structures (Hollis, et. al, 1997, 1997 and 1997).

OSCAR saw initial use on JWST (formerly NGST) and was expanded to include segmented optics (Lyon, 1998) and some levels of closed-loop control (Murphy, 2001). The segmented optics PSFs were used to test wavefront control approaches for JWST's DCATT testbed (Lyon et. al 1999) ultimately built by Ball Aerospace and Technology. It has seen periodic use on JWST to model the NIRCAM coronagraphic response.

OSCAR was used to develop the forward model for PRF for NOAA/GOES satellite image deconvolution; it was validated using measured GOES PRF data and deconvolved images were validated using higher resolution AVHRR satellite imagery collected at the same time and location on Earth (Lyon 2001, Howard 2001).

In 2001 and following OSCAR was expanded to handle multiple beam paths and partially non-sequential raytrace and diffraction for the purpose of modeling interferometers and was used to model the Solar-Viewing Interferometry Prototype (SVIP) (Lyon 2004), Fizeau Interferometry Testbed (FIT) (Carpenter 2003) and to synthesize data for testing various image construction approaches on the Wide-Field Imaging Interferometry Testbed (WIIT) (Lyon 2012).

OSCAR has been in a continual state of evolution since 1988 and growing in its capabilities since its inception. It is primarily used by R. Lyon as his prime tool for optical modeling but has been used by others. It has high fidelity optical modeling but limited graphics support. Most of the output datasets are either in FITS format or text format and other well developed graphics packages can be used to display them.

Since TPF-C days and thereafter OSCAR has continually added in various coronagraphic modeling capabilities such as external occulters, focal plane and Lyot stop masks, both continuous and segmented deformable mirrors, and various forms of the visible nulling coronagraph and both open and closed-loop control (see e.g. Lyon, 2007, 2012, 2012). OSCAR was used on 5 of the NASA/Astrophysics Strategic Mission Concept Studies (ASMC).

In this VNC SAT/TDEM effort OSCAR was used to model, along with analytic modeling (Section 2.3.1), to allocate the values for the lab VNC error budget (Table-3) that were traceable to flight requirements (Table-2). The surface quality of the VNC surfaces were measured using a Zygo interferometer and over the region of the beam foot print (<1 cm) the surfaces were all significantly better than the allocation and all were less $\lambda/100$ rms wavefront error after removal of tip/tilt and focus.

An OSCAR model was developed previously for the EPIC proposed flight mission, including the flight VNC (Clampin 2009). An OSCAR model has been developed for this milestone effort: for deriving the plate scale (section 2.3.3), for diagonalizing the control basis (section 2.3.4), and for developing and advancing the wavefront sensing and control

algorithms (section 3). The simulated performance of the lab VNC agrees with the actual measured performance in terms of contrast at IWA giving increased confidence that the modeling is useful for: the design process, algorithm development, and performance prediction for future VNC work and for proposed EPIC and/or other flight missions. Additionally models within OSCAR are applicable to a multitude of possible coronagraphic approaches and wavefront control strategies. Future efforts would benefit from continued model development, cross-validation of the model against milestone results, and release of the modeling tool for community wide use.

2.3.6 Difference Between Flight VNC and Lab Vacuum Nuller

There are several differences between the lab demonstration and the flight implementation: single nuller vs. dual nuller, wavefront control dynamic range, spacecraft pointing control, and polarization control.

Single Nuller: The proposed EPIC flight version of the VNC contained two nullers in series, nominally referred to as the X- and Y-nullers, each with differing requirements on their level of nulling and hence contrasts. A single nuller has two output channels known as the bright and dark channels, whereas the two nullers in series has in total three output ports each with its own detector. There are not four output ports since the dark output channel of the 1st nuller serves as the input of the 2nd nuller. The dual nuller yields a $\sim\theta^4$ null at 45 degrees to the XY axes of the nuller. A single nuller gives a $\sim\theta^2$ null. Milestone #1 for this lab demonstration used only a single nuller to reach 10^{-8} contrast.

Wavefront Error Dynamic Range: The EPIC optical telescope element (OTE) contributes wavefront errors of which a portion (due to shearing) of this wavefront shows up as a difference wavefront between the two arms of the nuller. The lab demonstration will not attempt to duplicate the wavefront errors expected from the EPIC OTE; this will be considered at a future date and would require a separate telescope emulator.

Spacecraft Pointing Control: The EPIC spacecraft has an attitude control system that body points to the target star and maintains pointing throughout an observation. The VNC controls local piston, tip, and tilt differences between the two arms of the VNC and in the laboratory environment pointing jitter is actively and passively controlled to less than 0.7 arcseconds rms using an active air table upon which the vacuum tank rests, passive isolators under the feet of the tank, and passive isolators between the VNC and its support structure within the tank. The pointing induced jitter will be considered at a future date.

Polarization Control: To achieve Milestone #1 the lab VNC uses a linear polarizer just following the input beam, 2 additional polarizers (one per arm) in the nulling interferometer, and a polarizer in the bright pupil channel output and a polarizer in the dark in focus channel output. A prism arrangement is initially used to ensure the polarization axes are aligned. The polarizers in each arm are subsequently fine tuned to balance the mean intensity in each arm of the interferometer. The polarizers reduce the throughput by 50% for randomly polarized light. The flight system will not utilize the polarizers due to an approach that mitigates their need and nulls both polarization states

simultaneously and that pushes the throughput close to 100% over the spectral bandpass. A follow-on SAT/TDEM to this work was awarded for Milestone #2 (discussed in section 7) to test this approach to achieve 10^{-9} contrast, with high throughput, in 7.5% spectral bandpass.

3. Milestone Procedure

3.1. Top-Level Description

Milestone #1 requires laboratory intensity measurement of light in the dark focal plane *after suppression* relative to the intensity in the dark focal plane *without suppression*, and as a function of focal plane location and beam shear to set the desired IWA.

For the lab VNC *without suppression* refers to driving both the delay line mechanism and MMA such that the detector counts at the center of the dark focal plane image is maximized, i.e. no nulling and results in an image on the dark channel detector as shown in Figure-19 left panel. *After suppression* refers to driving the piston mechanism and MMA to minimize the detector counts at the specified off-axis location in the focal plane and results in an image as shown in Figure-19 right panel. The ratio of the peak of the image between with- and without- suppression is $\sim 10^{-4}$ to 10^{-5} as shown in Figure-20 right panel at the center of the focal plane, i.e. at $0 \lambda/D$. Thus left- and right-images of Figure-19 are shown on different scale in brightness per this ratio. The specified off-axis location is at the angular separation where the measurements were made, i.e. at $2 \lambda/D$, and extending over a circular mask of diameter $1 \lambda/D$ centered on $-2 \lambda/D$ (red circle on Figure-12 lower left). At the VNC's plate scale of $0.06778 \lambda/D$, $2 \lambda/D$ falls at $2/0.06778 = 29.5$ detector pixels and the diameter of the mask is 14.75 detector pixels. The number of pixels within the mask is 166. However, we have measured both inside and outside of $2 \lambda/D$ also.

The contrast is estimated from $C(\theta) = F_{\min}/F_{\max}$ where F_{\min} is the measured photoelectron count in the detector pixel at focal plane location θ , *after suppression*, and F_{\max} is the measured photoelectron count at the on-axis detector pixel, *without suppression*, and where each is averaged over the contrast mask (red circle Figure-12 lower left). This is the reported contrast for each realization of each of the 4 DCE's. A "realization" consists of 200 closed-loop control steps with an auto-regressive moving average (ARMA) approach to feeding back the actuator voltages to minimize the effect of photon noise. A single realization consists of averaged contrast maps over 200 closed-loop control steps.

At the top-level, the measurement process consists a sequence of a two-cycle process. The first step, known as the *bright cycle*, refers to driving the piston mechanism plus MMA such that the on-axis flux is maximized, collecting a set of $M=4$ images while holding the maximum using the wavefront control – this is done before each realization. The second step, known as the *dark cycle*, refers to driving the piston mechanism plus MMA such that the off-axis flux is minimized, collecting a set of $N = 200$ images while

holding the off-axis counts, averaged over the dark hole mask (blue region on Figure-12 lower left) at the minimum using wavefront control.

While collecting this set of 'raw' images, with and without suppression, wavefront control is operating in closed-loop. Wavefront control uses simultaneously both the dark and bright channel camera images, plus the control algorithm to generate delta-voltages to feedback to the piston mechanism and MMA. A simulation of this process is shown in Figures 18, 19 and 20. Figure-17 left shows the initial wavefront error (random PSD of form $\sim 1/f^3$ and Figure-18 middle 2nd shows the sensed WFE over the region of common beam overlap defined by the shear, pupil stop and MMA. Sensing is accomplished by jointly solving for the errors using both the bright channel (at or near pupil image) and dark channel (in focus) images. Figure-18 right shows the residual wavefront error after correction. At the outset of the measurement process a series of bright images is collected and are averaged to determine the peak for the contrast calculation, i.e. the denominator in equation-2. This detector is an E2V-L3 and has the capability to count individual photons and has excellent linearity⁸ of $< 1\%$ and \sim zero readnoise.

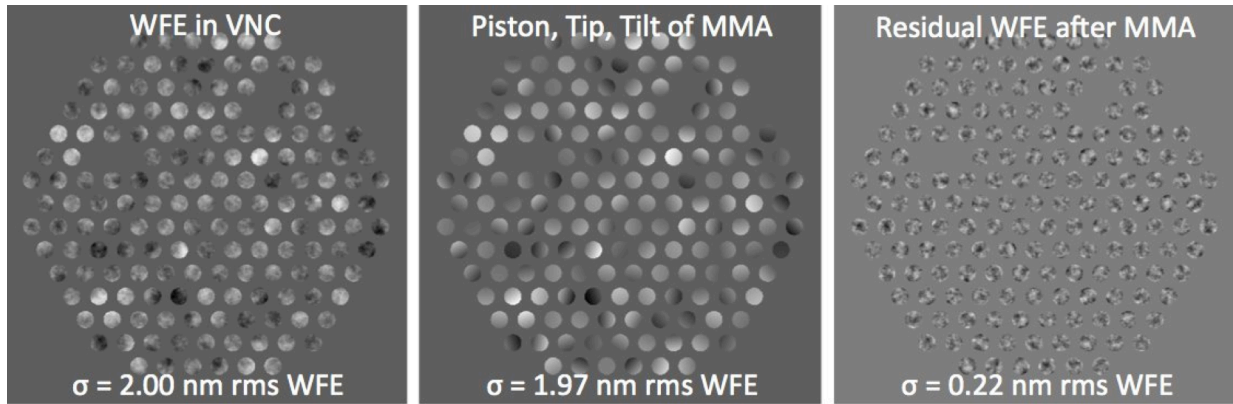


Figure-18: Simulation of Wavefront Control Sequence

(Left) Initial WFE input to VNC, (Middle) Sensed wavefront decomposed in terms of piston/tip/tilt on each MMA segment, (Right) Residual WFE. Residual WFE of 0.22 nm higher spatial frequency than initial WFE.

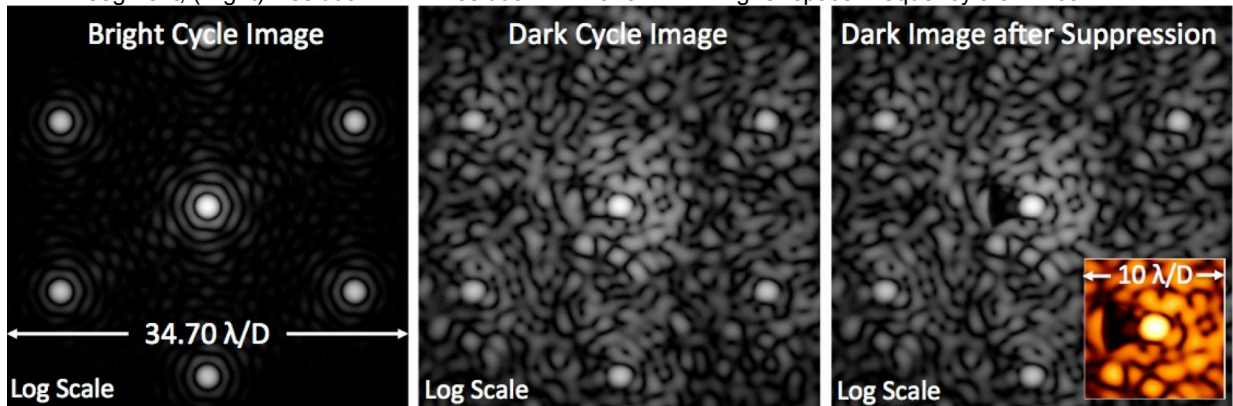


Figure-19: Simulated Focal Plane Images and Coronagraphic Hark Hole

(Left) Bright channel image on 16-bit 512x512 detector with 0.06778 λ/D sampling; this with dark channel image used jointly to solve for WFE, image from driving delay line to maximize brightness. (Middle) Dark channel image on detector, i.e. SCI focal plane, with 0.06778 λ/D sampling, image results from driving dark output channel to be as dark as possible and occurs during dark cycle; speckle becomes evident, (Right) Dark channel image on detector, i.e. SCI focal plane. This image results during dark cycle but following control with the MMA. Dark hole is dark region in to the left of image center and the inset shows a 10 x 10 λ/D . Milestone #1 at 2 λ/D or 29.5 detector pixels to the left of the image center (bright core).

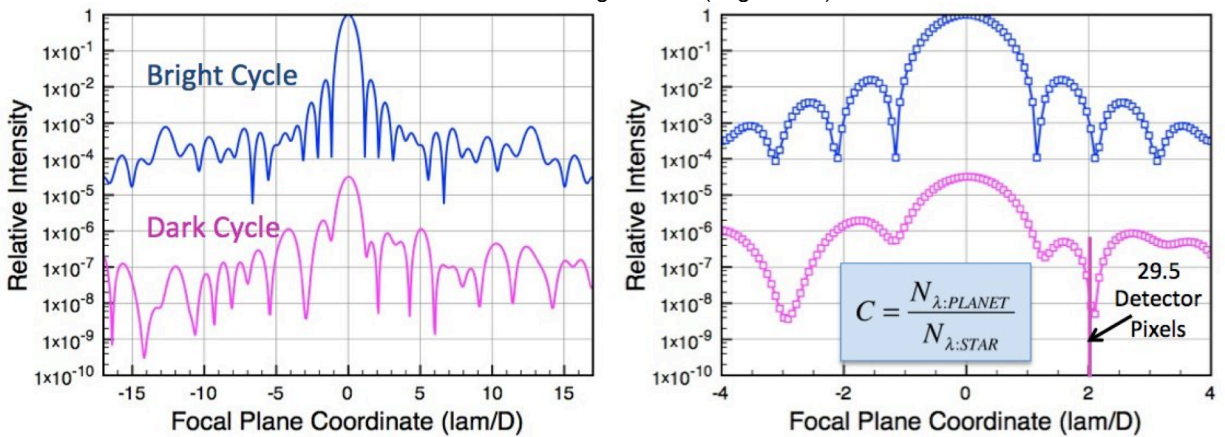


Figure-20: Plots thru both Bright (Fig-19 left) and Dark cycle (Fig-19 middle) science focal plane. Left plot is from left-to-right through image center of Fig-19 (left) and subtending the full 34.70 λ/D detector field of view, and. The right plots over a smaller 8- λ/D field of view with the number of detector pixels to 2 λ/D labeled. The sampling in this simulation is the same as the VNC detector at 0.06778 λ/D or 14.75 detector pixels per λ/D .

3.2. Detailed Description

The contrast measurement requires a measurement of the focal plane intensity averaged over the area of a single detector pixel and over successive time windows as discussed above; statistical measures are used to assess confidence and to minimize the impact of noise and uncertainties. The following sections 1st give a series of definitions and subsequently delineate the detailed step-by-step procedure for the measurement process, and call out the data products.

3.2.1. Raw and Calibrated Images. “Raw” images are the pixelated images directly output by both the bright channel CCD and the dark channel detector. The bright CCD images are in units of analog to digital units (ADU), i.e. detector counts, and the dark channel images are in units of photon counts. The 16-bit camera is operated at or near 80% full well to avoid near saturation and nonlinear effects. “Calibrated” images are processed in-situ to subtract dark frames and by flat fielding in a standard well-understood process. The aggregate set of ‘raw’ and ‘calibrated’ images that were used to achieve Milestone #1 are archived in an off-line set of CDs and will be available for further analysis as required.

3.2.2. “Contrast Images” are defined by $C = \frac{F_{\min}}{F_{\max}}$ where F_{\max} and $\frac{F_{\min}}{F_{\max}}$ are the calibrated values from 3.2.1 and are the images used to estimate the reported contrasts.

3.2.3. “The VNC Control Algorithms” are defined to be the sequence of steps shown in Figure-21. The coarse phasing algorithm brings the VNC from potentially mm’s to <200 nm rms. The tuning algorithms further phases the systems from ~200nm rms WFE to ~0.068 nm rms WFE, and then holds the WFE at ≤ 0.068 nm rms WFE (per the error budget in Table-3). It should be noted that this is equivalent to an effective WFE of 0.202 nm rms when integrated over 2x (for Nyquist) the spatial frequencies defined to the outer edge of the focal plane mask, or 4.0 cpa ($4 \lambda/D$) in the focal plane (Figure-14). Contrast measurements are only made while under dark channel control (see step 6 of Figure 21).

The algorithmic steps shown in Figure-21 are designed to operate as a cascaded servo: each algorithmic step transitions to the next as a weighted sum of the current algorithm and its predecessor. It should be noted that wavefront control is accomplished from the pupil and focal planes and no discrete optics are moved into or out of the system during operation of the algorithmic steps. The only moving components are the individual mirror segments of the MMA, and the piston mechanism which moves over a maximum range of ~160 nm during closed-loop operation.

Algorithm (2) is rapid and is just applying a look up table to the MMA. Algorithm (3) moves the delay and uses a variation of Bucket (or ABCDE) interferometry algorithm - typically takes several minutes to bring the rms WFE to ~20 nm. Algorithm (4) takes approximately 1 minute and is mostly concerned with tuning overall beam focus and segment level piston/tip/tilt to better place the focal plane image. Algorithm (3) and (4) are iterated several times thereby moving both MMA segments and delay line but such that the average delay line offset is approximately the average over the set of MMA

pistons, this insures that the DM segments are at or near the center of their range to maximize control dynamic range. Algorithm (5) is several minutes and is used to drive the pupil dark and to collect the bright frames in the focused image for contrast calculation. At the end of algorithm 5 the MMA is moved in pure piston to invert the dark pupil to a bright pupil and thereby darkening the focal channel image – small tuning of the MMA is also required to make the bright pupil image as bright as possible. At this point the handoff to the fine control is initiated by running the dark channel modal control that moves linear combination of actuators to build the dark hole and progressively lower its mean counts over the region of the mask and to hold it as dark as possible. This is more time consuming and takes ~20 minutes to lower the dark hole below to $\sim 10^{-8}$. If a large disturbance is encountered resulting in an out-of-spec condition it damps itself out and ramps in its predecessor algorithm.

All algorithms are implemented in C/C++ with threading in a Windows environment with cameras, mechanisms and MMA running on different threads. We are currently working on implementing it a Linux based real time operating system that controls through multi-threaded C/MPI code and this is functional except for the MMA – we are awaiting delivery of the MMA Linux driver from IRIS-AO. The control algorithms feedback delta-voltages from the current voltages for the MMA and piston mechanism where the delta-voltages are calculated both for MMA and piston mechanism but with a series of constraints to maintain the temporally filtered mean (averaged over the set of MMA segments) MMA piston at zero and shifting this low-frequency filtered mean piston to the more coarsely controlled piston mechanism at lower bandwidth. The MMA voltages map ~quadratically to MMA motion and this is folded in as part of the control algorithm. All control algorithms are performed at the same spectral bandpass and with the same images used to actually calculate the contrast and thus the control and the desired measurement, contrast, are well mapped to one another.

3.2.4. Data Collection Event

A data collection event (DCE) is approximately 3.47 hours in length and includes as its final segment one 950 second sequence of 3,800 512 x 512 images. The 950-second interval is the aggregate time of when algorithm (6) (Figure-21) is used for contrast and does not include the times for algorithms (1) through (5). A DCE is longer than 950 seconds but only the last 950 seconds are used for the milestone since the earlier times is spent in coarser phasing and building the dark hole.

Using the calibrated data obtained during fine control at 4 Hz [Figure-21, algorithm (6)], contrasts were calculated - shown as algorithm (7) in Figure-21. It was found that the initially proposed approach of cycling between bright and dark time windows is not viable since it introduced instability into the control and that it was more efficient to first collect a set of bright images and average them, followed by controlling to build the dark hole by iteratively cycling through the diagonal control modes and subsequently holding the dark hole by calculating a metric as the mean contrast over the region of the dark hole and moving control modes to compensate.

The bright images, i.e. w/o suppression, the mean photoelectron counts in the center pixel of the unsuppressed image were calculated from $F_{\max} = \langle I \rangle = \frac{1}{M} \sum_{j=1}^M I_{j\Delta t}(0,0)$ where $j\Delta t$ is the time index extending to M-frames and $I_{j\Delta t}(0,0)$ is the intensity in photoelectrons at the peak image pixel. The population standard deviation was calculated and the standard error of the mean calculated from $\varepsilon = \sigma_I / \sqrt{M}$ and M was selected such that the standard error is < 0.1 detector count, resulting in $M \sim 5000$.

The contrast for each time is calculated from:

$$C_k = \frac{\langle I_{\min} \rangle_k \pm \varepsilon_{k:\min}}{\langle I_{\max} \rangle_k \pm \varepsilon_{k:\max}} \approx \frac{\langle I_{\min} \rangle_k \pm \varepsilon_{k:\min}}{\langle I_{\max} \rangle_k} \text{ for } k = 1, \dots, 200 \quad (8)$$

Where $\langle I_{\max} \rangle_k \pm \varepsilon_{k:\max}$ are the on-axis (unsuppressed) photoelectron counts, with standard error, and $\langle I_{\min} \rangle_k \pm \varepsilon_{k:\min}$ are the off-axis (suppressed) photoelectron counts, with standard error, at $2 \lambda_o/D$ and this is the number reported on as the milestone. However, the control metric is actually the mean counts over the region of the mask (see section 2.3.4 and Figure-14) The signal is large for the unsuppressed photoelectron counts and thus the error on the mean contrast is dominated by the noise in the suppressed photoelectron counts. Thus contrast, with error bars, for the last 3,800 frames of a DCE spanning 950 seconds is also calculated and reported.

The single side upper confidence limit is given by $UCL = C_k + A \frac{S_k}{\sqrt{N}}$ and where A is constant derived from Student's t-distribution for a 90% confidence and given by $A=1.33$, and S_k is the population standard deviation over the set of 200 samples. Thus the requirement for 10^{-8} contrast is met when $C_k + 1.33 \frac{S_k}{\sqrt{N}} \leq 10^{-8}$ to a 90% confidence level.

In principle the bright output camera could be used to also perform the no-suppression cycle of the data collection event, and this would remove the need to interleave between

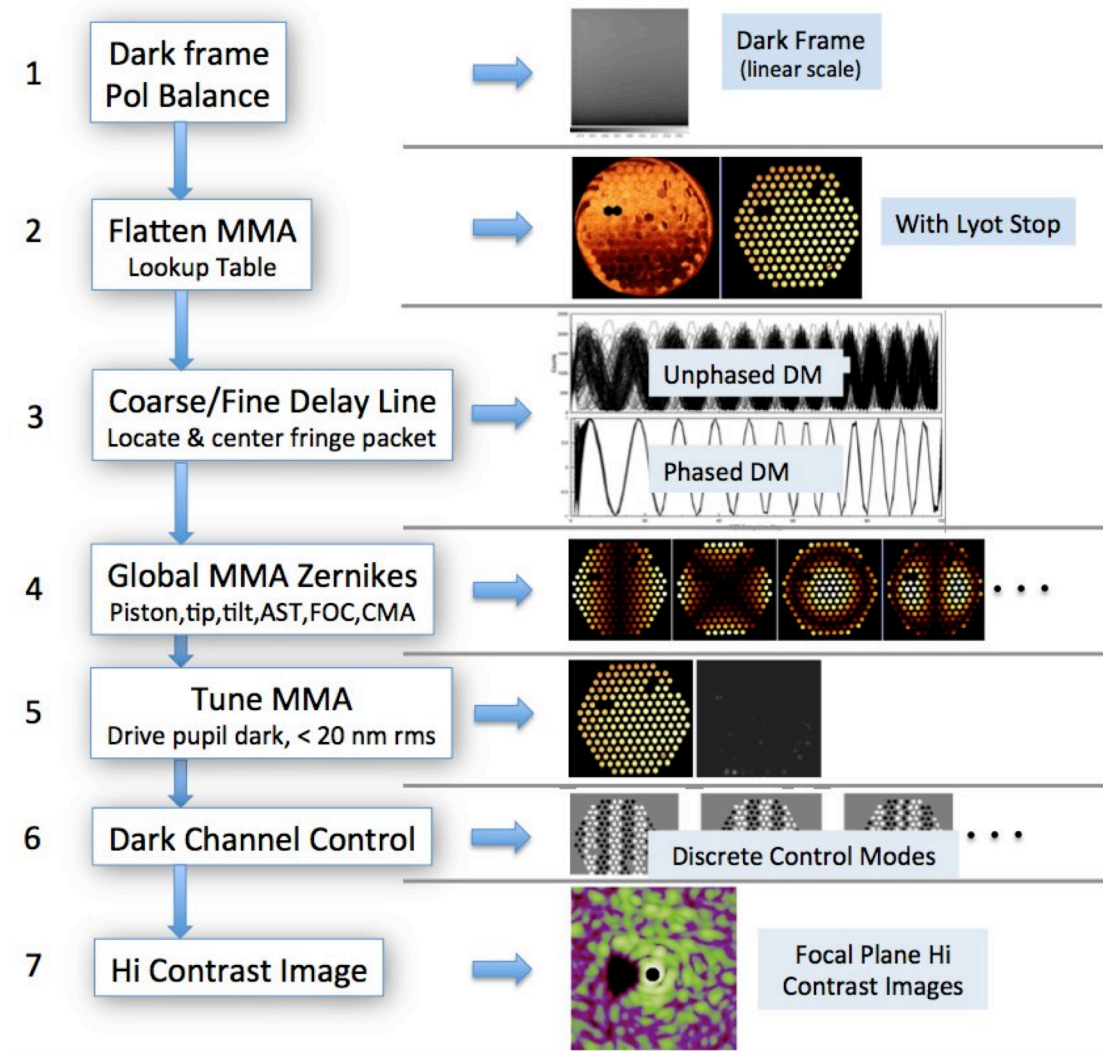


Figure-21: Null Control Sequence (described in the text)

bright and dark image sequences. However, with the current lab testbed setup the bright and dark cameras have deliberately different characteristics since during fine control the bright output channel sees out of focus 16-bit images for wavefront control and cross-calibration between the two different cameras would be difficult.

3.3. Focal Plane Contrast Measurement Steps

The focal plane contrast measurement steps are described in this section, and this section has been revised from the whitepaper. This was deemed necessary as the sensing and control of the VNC and MMA has significantly advanced since this effort was proposed.

All output images were saved during the Calibration sequence and during Algorithms (1) and (2) as FITS files, however during fast closed-loop (algorithm (3)) all images were not saved as the time to collect, format, and write images to a disk file appreciably lowers the closed-loop control bandwidth from its nominal value of 40 Hz. These images were only saved at the rate of ~ 1 per 0.25 seconds.

3.3.1 Initialization: Initialization consists of first turning on the source, vacuum pump, the cameras and camera chillers, then waiting for the system to stabilize. Next the MMAC and piston/shear mechanism are switched on, and the data processing interface to these systems booted. The MMA is then commanded to a preset ‘flat’ setting that has been pre-determined to off-load substrate bowing to nominally set all MMA segments to provide a composite WFE < 60 nm rms. The piston mechanism is then set to about the middle of its travel. When operating in narrowband light the range is \sim cm’s due to the long coherence length. Then shear mechanism is then moved ~ 2.5 mm to deliver 1/4 beam. Following these initialization steps the system is considered to be in its *initial state* and the first contrast field image is collected.

3.3.2 Null Control

The null control sequence consists of the series of 7 high-level steps shown in Figure-21. The null control sequence uses images from the bright pupil camera and dark focal plane camera to both reduce the mean and the rms wavefront error (WFE) and subsequently control a specific range of modes (spatial frequencies) to obtain and hold a dark-hole at a specific location in the focal plane. The mean WFE is the piston difference between the two arms of the interferometer and it controls the overall irradiance of the dark focal plane image. The ideal mean wavefront error is half a wavelength of light, i.e. $\lambda/2 = 316.4$ nm; this would result in perfect nulling monochromatically if no other error sources were present. In practice we set and hold it to 316.4 ± 6 nm, where $\lambda = 632.8$ is the center wavelength of the bandpass. This is sufficient to achieve center nulling of the core of image to < 0.001 . The remaining control sequence steps lower the rms wavefront error over a range of spatial frequencies sufficient to burn a dark-hole $\leq 10^{-8}$ for inner working angles from $1.5 - 4 \lambda/D$.

1. Polarization Balance & Dark Frame: Polarization balance corrects the mean intensity difference between the two arms of the interferometer to $< 1\%$. This is accomplished by a linear polarizer before the first beamsplitter, one linear polarizer in each of the two interferometer arms, and a linear polarizer after the beam combining beamsplitter at each of the cameras, i.e. five linear polarizers in all. All the polarizers are set to the same axis before insertion into the interferometer. A sequence of images are collected with both interferometer arm shutters closed followed by a sequence with one shutter open and another sequence with the other shutter open, i.e. only one shutter within the interferometer is open at a given time. Each of the image sequences is averaged and the detector counts totaled and the mean difference tabulated. This is repeated after rotating the polarizer in the interferometer arm with the greatest intensity to match the arm with the lower intensity. This is repeated until balanced as best as possible. Dark Frame is a fairly standard calibration approach for the cameras and consists of collecting frames with the source off (bias frame), source on but shutters closed (dark frame), and ramping

the integration time to obtain the gain (photo-electrons/ADU) for each camera pixel. This calibration was performed at the outset of the data collection events.

2. Flatten the Multiple Mirror Array employs a lookup table to command each of the segments in piston, tip and tilt to nominally minimize the WFE between the two interferometer arms. The lookup table is periodically generated by using a 5-bucket interferometer algorithm [see e.g. de Groot (1995) and references therein]. At this step the WFE is typically 20 – 40 nm rms. The spread is caused by slow thermal drift in the optics mounts; a newly generated lookup table gives ~20 nm rms whereas after 3 or 4 days it has drifted up to ~40 nm rms.

3. Coarse & Fine Delay Line refers to moving the mechanical delay followed by fine tuning with a piezo mounted on the head of the mechanical delay line. The mechanical delay uses a straightforward approach that steps the delay line along continuously but such that the bright pupil images is sampled at intervals of ~300 nm resulting in a pupil image at each time step. Significant modulation of this image results when the path difference between the interferometer is less than the coherence length of $\lambda/\Delta\lambda \sim 0.3$ mm and fringes become visibly evident in the pupil camera. The variance of the counts of images within the coherence length is higher than when outside the coherence length and this is exploited to set the coarse mechanical delay such that the path differences are within the fringe packet. Once at this position, the fine delay line is stepped in ~20 nm increments over the entire fringe packet group (Figure-21, to the right of box labeled Coarse/Fine Delay), and a Hilbert transform algorithm is used to estimate the central fringe location.

4. Global MMA Zernikes refers to using low order spatially correlated Zernike polynomial modes imposed by moving the MMA segments individual piston, tip and tilt actuators to match the core of the point spread function (PSF) in the interferometer arm with the MMA to the core of the PSF resulting from the other arm of the interferometer. Global piston, tip, tilt, astigmatism, focus, coma, trefoil and spherical aberration Zernike modes are used in a Likelihood type metric with a non-linear function minimization to minimize the rms counts in the core of the PSF. This effectively lowers the core of the PSF to $<10^{-4}$ of the incoherent sum of each, i.e. relative to the un-nulled image.

5. Tune MMA: refers to moving individual segments of the MMA in local piston, tip and tilt, to minimize the counts in the pupil image, i.e. to drive it as dark as possible to the noise floor of the camera. These motions are constrained to move only a few nm from their starting positions by a constrained optimization. The constraints insure that the control does not stray far from the starting position during gradient calculations performed by dithering each segment. After tuning the wavefront error is < 20 nm rms. Immediately following this a $\frac{1}{2}$ wave shift is imposed by moving each MMA segment in piston only, this inverts the pupil image from dark to bright irradiance and a few iterations are used to drive this image as bright as possible. Internally the driving to dark then driving to bright is run in closed-loop.

6. Dark Channel Control: Up to this point the control has been entirely accomplished using only the images from the pupil camera and results in a wavefront error of <20 nm rms and a mean wavefront error of <6 nm and the core of the PSF has been reduced by $\sim 10^4$. At this point fine modal control takes over. This operates by recognizing that only a limited number of control modes are needed to control most of the power within the dark-hole region. The number of control modes is reduced to less than 200 per the discussion in section 2.3.4 and reducing the modes is based on using those linear combination of actuators that result in the largest change in mean counts in the region of the dark hole. In practice, the number of possible motions is reduced by designing a lower rank orthogonal basis. The number of basis vectors is reduced by defining a region or patch of the focal plane where high contrast is desired and calculating the response of the electric field for each basis vector (eigenvalues) and sorting on the eigenvalues in descending order and using only those basis vectors (eigenmodes) that give appreciable gain. Those modes that give little gain generally affect the result at or below the noise floor, i.e. the noise floor defines where the eigenvalues are cut off. This approach uses standard linear algebra techniques to find the eigenmodes for a given focal plane region. Some of the lower order modes for a region extending from $1 - 5 \lambda/D$ are shown to the right of 6. Dark Channel Control in Figure-21 (Figure-15 shows the first 25 control modes of the 200 modes we used to achieve the milestone), and to achieve contrasts of 10^{-8} requires only ~ 200 modes (Figures-16 & 17). In the control system these modes can be implemented rapidly in the control loop since, in the small angle approximation, it is only a dot product with a region of the focal plane image.

7. High Contrast Image: The steps 1-6 results in a high contrast image as shown in Figure-22, and starting from scratch for each DCE shows that the approach is stable and repeatable.

Each step in the process is designed to introduce less spatial correlation in the wavefront error across the pupil, e.g. moving the delay only imposes a global wavefront change across the entire pupil, while moving global Zernike modes imposes wavefront changes that vary across the pupil but with long correlation lengths, i.e. low spatial frequencies, and moving of the discrete modes controls a narrow range of spatial frequencies, and individual MMA segments have the shortest correlation length and hence control the highest spatial frequencies. This approach effectively bootstraps from lower to higher spatial frequencies

3.4. Milestone Validation Procedure

The procedure for the milestone demonstration is as follows:

3.4.1. The Lab VNC is set to its initial state per Sec 3.3.1. The IWA is adjusted for $2 \lambda/D$. An initial coronagraph contrast field image is obtained, as described in Sec. 3.3.

3.4.2. The control algorithm is used to find the settings of the DM actuator driver voltages that give the required high-contrast in the target dark field.

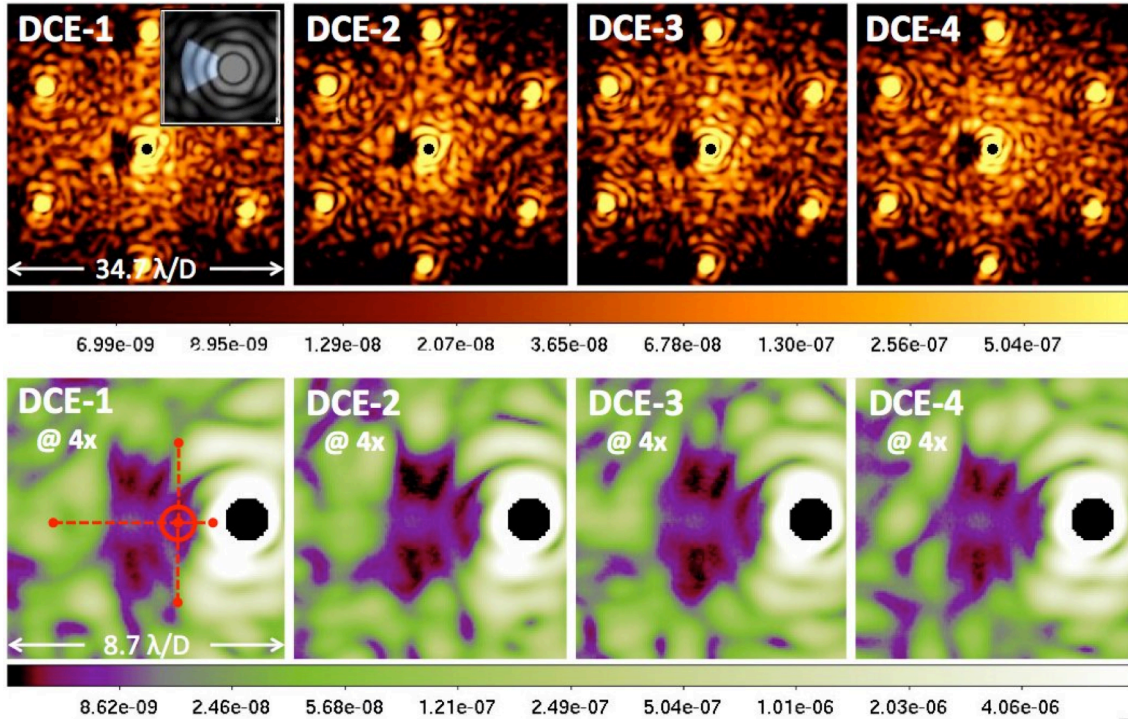


Figure-22: Contrast Maps. Top row shows resulting average contrast maps from each of four different data collection events (DCE) on a log and color stretched scale to accent residual structure. The upper left image contains an inset of the dark-hole control mask, at 2x scale, in light blue – the pie shaped region left of center is the region over which the control modes are diagonal. Bottom row are the same images as the top but zoomed by a factor of 4x and shifted to right, and different color maps, to further accent the dark-hole region. The central core is numerically (dark circle) masked to compress the image dynamic range for display purposes. The open red circle on the lower left panel shows a $1\text{-}\lambda/D$ diameter mask centered on $-2\lambda/D$ – this is the region over which that the contrast and its statistics are calculated for this milestone. The left-to-right dashed red line is the location and length of the plots in Figure-23, and the north-to-south dashed red is referenced on Figure-24.

3.4.3. Data Collection Events are acquired, as described in Sec. 3.2.4, each comprised of 1000 seconds of data with 200 contrast measurements. *Actual time in the lab was 950 seconds.* The DM actuator driver voltages are continually adjusted while this sequence of contrast images are collected to hold required contrast.

3.4.4. Laboratory data are archived for future reference, including raw and calibrated images of the reference star and contrast field images.

In addition to narrowband contrasts reported at $2\lambda/D$ we will report on contrasts, with error bars, at 1, 2, 3, 4, 5 and 6 λ_o/D while the IWA is still set for $2\lambda/D$ in the focal plane shear direction, i.e. along focal plane direction across the transmission fringes. This maps the contrast behavior as a function of focal plane location with the inner working angle set for a planet at $2\lambda/D$ and provides the size of the high contrast region over which a planet could be found for a particular optimized IWA. Additionally it quantifies the contrast inside the IWA where theoretically it would be possible to look for a planet.

We will also optimize the shear separately for 3 and 4 λ/D and report on the contrasts with error bar from 1 – 6 λ/D . This maps the contrast behavior as a function of shear

and demonstrates that the shear can be optimally tuned for the location of a known planet such that it could be spectroscopically characterized. It is not critical to meeting milestone #1 and will be performed as resources permits.

4. Success Criteria

The required elements of the milestone are as follows: Each element includes a brief rationale.

4.1. Illumination is narrowband light (<1% spectral bandpass) with a single linear polarization at a wavelength centered on 632.8 nm realized by an interference filter on a broadband source.

Rationale: This milestone is a narrowband experiment to demonstrate feasibility of the approach at a wavelength in the science band of EPIC.

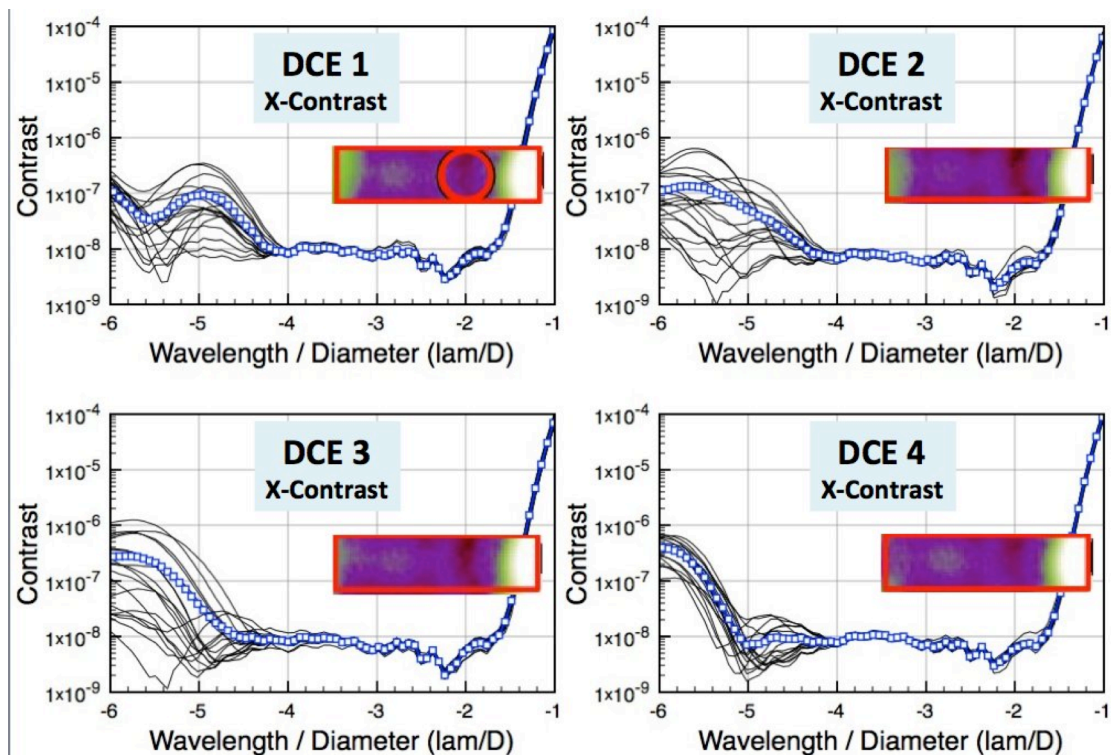


Figure-23: Contrast Plots in X-direction for 4 DCEs. Each plot shows contrast versus angular separation for the 19 realizations (black) and average of each 19 realizations (blue with square markers). Each plot is aligned with the left-to-right red dashed line in the lower left panel of Figure-22. The primary region of interest for this milestone is the $1/\lambda/D$ width region surrounding $-2 \lambda/D$, shown as the red circle in inset of upper left plot. Rectangular insets show a region extending from -6 to $-1 \lambda/D \times 1 \lambda/D$. An average of the samples from -2.5 to $-1.5 \lambda/D$ on the plots does not properly show the milestone contrast at $2 \lambda/D$ since the proper averaging is in $2D$ – over the circular region, i.e. there are few samples are at the inner edge of the circular $1 \lambda/D$ mask. For each of the 4 plots the contrasts, averaged over the $2D$ red circle (per the milestone), are shown in Figure-25 and tabulated in Table-5 and discussed in Section 5.

4.2. The mean plus 1.33 of the standard error of the contrast is less than 1×10^{-8} at a where the mean and standard error are calculated over a circular region centered $2 \lambda/D$ of diameter 1λ ; this region contains 75 detector pixels. Each of the 4 Data Collection

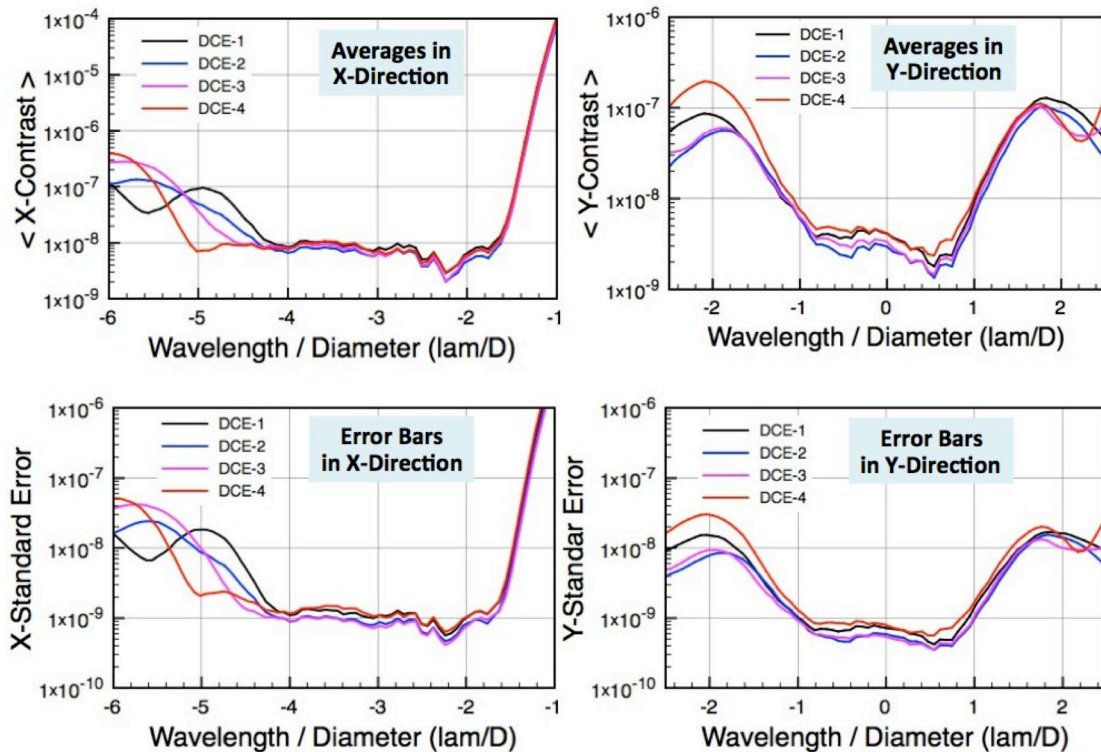


Figure-24: Average Contrast Plots with Standard Errors in X and Y. Top row shows plots over average contrast versus angular separation in X and Y respectively. The position of the plots corresponds to the X and Y red dashed line in Figure-22 and the plots cross at $-2 \lambda/D$ in the X direction, i.e. the contrast values at $-2 \lambda/D$ in X and $0 \lambda/D$ in Y are the same. The bottom row shows the standard error of the mean, i.e. the error bar on the average contrasts from the top row. The averages are calculated of the 19 realizations per DCE and the error bar is the population standard deviation divided by square root of 19.

Events (DCE) spanned 950 seconds of data-collection, comprising a total of 76 contrast estimates (19 per each of the 4 DCEs). These estimates are reported as a function of time in Figure-25.

Rationale: This provides evidence that contrasts approaching those needed for achievement of science can be met to a 90% confidence limit for times that are comparable to expected drift rates on the flight mission.

4.3. Elements 4.1 – 4.2 must be satisfied on three separate occasions with at least 24 hours between the beginning of each demonstration.

Rationale: This provides evidence of the repeatability of the contrast demonstration.

5. Results

A complete DCE event consists of 500,000 images from the dark focal channel camera at 40 images (frames) per second (fps). The camera is displaying images on the testbed image display at ~ 40 fps, however, images are “grabbed” off the video stream at the

slower rate of 4 per second, then formatted as FITS files and saved to disk files. The 40 fps, however, are used internally by the control software by using a polynomial based ARMA model to define the weights and averaging process for the current frame plus the a weighted sum of the previous 10 frames. Thus the sampling frequency is 40 Hz but the control frequency is 4 Hz. The 40 fps is limited by the camera's frame rate. Each DCE consists of a total of 500,000 images of which only the 50,000 ARMA frames are formatted and stored as disk FITS files, i.e. 4 per second. Thus each single DCE is separated by ~24 hours from the other DCEs, consists 50,000 frames / 4 fps = 12,500 seconds or 3.47 hours per DCE. The first 46,200 images are required to construct the shape of the dark hole and achieve successively better contrast – after approximately 45,000 images the system has converged and contrast stabilized. The last 3,800 images are the best in terms of contrast and stability and it is these images that are retained and archived and used to report the contrast metric. The set of 3,800 images represents ~950 seconds of data. There are 200 control modes (Figure-17) and each control mode is sequentially stepped starting with the largest mode (maximal sensitivity) and continuing to mode 200 (least sensitivity). The controls software requires 200 control steps to move all 200 modes at 1-mode per step, resulting in $3,800 / 200 = 19$ full minimization steps of the control modes per DCE. *Herein we refer to each of 19 as a “realization”.*

The contrast is calculated for each of the 19 realizations for each of the 4 DCEs, 76 contrast realizations in all. An image is collected at each step and the MMA actuators are also commanded at each step. Thus we consider the first 46,200 images as part of initial wavefront control to achieve the final contrast, and the last 3,800 images (950 seconds) for holding the contrast and as the data used for assessing the contrast milestone. Each of the 19 realizations for the 4 DCEs are shown as a function of time in Figure-25. The dotted green line in Figure-25 is the mean over the 19 realizations for each DCE.

A single image at 40 Hz appears noisy due to few photon counts within the dark-hole region. However each of the 19 realizations per DCE actually consists of 38,000 total frames at 40 fps thus the standard deviation of the noise is lower by $\sim 1/200$. The source with the delay line set to null the bright pixel are set such that a contrast of 10^{-4} yields 80% of full well, or 52,428 analog to digital units (ADUs or detector counts) at the brightest detector pixel. The camera gain is 3 photons per 1 electron and thus the image peak corresponds to $\sim 160,000$ photons or an effective contrast dynamic range of 1×10^{-4} to 0.6×10^{-9} per realization. The 0.6×10^{-9} is the camera limited noise floor.

The milestone is based on the statistical ensemble of 19 contrast realizations per DCE. This metric is what is important for a flight coronagraph that runs WFC in closed-loop, since flight missions are likely to be photon starved for the exoplanet and would likely require significant averaging to detect an exoplanet.

Figure-22 shows the contrast maps from 4 data collection events obtained in the early AM the morning of June 8, 2012 through Monday June 12, 2012. These results were also reported on in Lyon et.al (2012). The top row shows the resulting 512 x 512 contrast maps. The center of each of the 4 contrast maps has a bright core (central region) with the peak pixels numerically masked for display purposes, with a dark region to the left of it. This dark region is the ‘dark-hole’ shown on a log scale to compress the visual dynamic range of the image. Visually there are also 6 separate sidelobe peaks due to the diffraction symmetry of the hex-packed MMA and each of these 6 peaks has a dark-hole to left of it.



Figure-25: Contrasts for each Realization of each DCE. Each of the 4 DCE's are on 4 successive days, each of which began in the early am – the dates for each DCE are shown along the abscissa. Each DCE consisted of 19 realizations; the contrasts averaged over the $1 - \lambda/D$ mask centered on $-2 \lambda/D$ are shown as blue boxes. The mask is the circular region shown as the open red circle on Figure-22 lower left panel. There are 166 samples with this region. The average over the set 19 is shown as the dashed green line for each DCE and the average contrast value is shown as $\langle C \rangle$ with error bars. The error bars are the population standard deviations over square root of 19. *The average contrasts, with error bars, are used to assess the milestone.*

These dark holes at the 6 sidelobe peaks are not as deep as the dark hole near the center, they would however, allow for higher contrast imaging at 6 locations of these secondary dark holes than that of the region surrounding each secondary dark hole: The size of the dark hole region is limited by the MMA segment count, the addition of more segments would yield a larger dark-hole region.

The contrast maps in the bottom row of Figure-22 are the contrast maps from the top row of Figure-22 but zoomed in by a factor of 4x to show a region 128×128 samples on a side and centered on $-2 \lambda/D$ and with a different color scale. It is seen from the color bar scale that the darkest regions are $<10^{-8}$ contrast. Figure-23 plots contrast in the x-direction for each of 19 realizations, and their average over 19, for each of the 4 DCEs. Each plot is aligned with the left-to-right red dashed line in the lower left panel of Figure-22. The primary region of interest for this milestone is the $1-\lambda/D$ region surrounding $-2 \lambda/D$ (red circle on Figure-22 lower left) and from the 4 plots it is seen that the average for each DCE is $<10^{-8}$. Figure-24 plots the average contrast over the 19 realizations per DCE in X (upper left panel) and Y (upper right panel) and their error bars in X (lower left panel) and Y (lower right panel). The X and Y plot locations, directions and length are shown by the X and Y red dashed lines on the lower left panel of Figure-22. The X and Y direction plots cross at $(X,Y) = (-2, 0) \lambda/D$.

The contrast maps in Figure-22 and the respective plots in Figures-23 and 24 show the contrast on a detector pixel-by-pixel basis in the region of the dark hole and shows high contrast in that region. However, what is directly relevant for the milestone criteria is that the contrast at $2 \lambda/D$ achieves the milestone. Contrast at $2 \lambda/D$ is not at a single sample, but at an average over the region defined by a speckle, regardless of sampling. We use a circular $1-\lambda/D$ diameter region of a speckle and for each the 19 realizations for each DCE average the contrast over that region (red circle on Figure-22 lower left), and we define the mask that defines that region as the contrast mask. These results of this are plotted in Figure-25 where the blue boxes are the contrast over the contrast mask for each of the realizations. The set of 19 contrasts are averaged and their standard errors to yield 4 average contrasts with error bars, one per DCE. The average value for each DCE is shown as the dashed green lines in Figure-25 and the 10^{-8} milestone contrast is shown, as a reference, as the wide green line along the top of the plot. The average contrast $\langle C \rangle$ and error bars are shown in the boxes on Figure-25. All 4 average contrasts are better

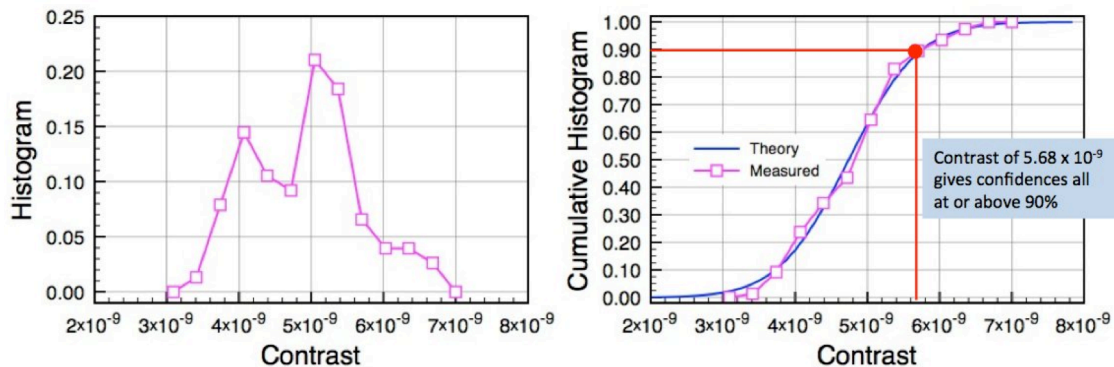


Figure-26: Histogram and Cumulative Histograms of Contrast at $2 \lambda/D$.

Left: Histogram of 4 DCE \times 19 realizations = 76 contrasts per Table-5 normalized to unit integral. Right: Cumulative histogram as estimator of cumulative PDF. Obtained by summing all contrasts below the contrast value shown on the abscissa. The theoretical cumulative PDF is also shown for 18 DOF (19 realizations – 1) for the mean and standard error in Table-5 lower right. Contrast at red dot (5.68×10^{-9}) is the value that represents 90% confidence, and agrees well with the theoretical curve.

than 10^{-8} and fall at least 34 standard errors below the milestone contrast implying high confidence.

Table-5 shows the relevant statistics for each of the 19 realizations for the DCEs. The first column indexes the contrast realization. Columns 2 through 5 lists the *Average Contrast @ $2 \lambda/D$* where the average is performed over the contrast mask. Just below the list of contrasts for each DCE is the row of average contrasts over the set of 19 contrasts and shown in green font. Below that is the population standard deviation, σ , and below that the standard error of the mean given by $\sigma/\sqrt{19}$ also shown in green font. Thus the average contrast, e.g. for DCE-1, is $5.51 \times 10^{-9} \pm 1.30 \times 10^{-10}$. Students-t is the number of standard errors the mean contrast is less than the hypothesized contrast, i.e. milestone of 10^{-8} , and is given by $t = \frac{C_h - \langle C \rangle}{\sigma/\sqrt{N}}$ where C_h is the milestone contrast. The t-value follows

Students t-distribution and the cumulative distribution function allows assessment of confidence (see e.g. [http:// http://en.wikipedia.org/wiki/Student's_t-distribution](http://en.wikipedia.org/wiki/Student's_t-distribution)). For the 4 DCEs the average contrasts each are significantly better than the required milestone contrast and all have confidences greater than 99.99% - exceeding the 90% confidence limit set as the success criterion for the milestone #1. Thus each of the 4 DCE's exceeded the required contrast and conference limits for this milestone.

Figure-26 (left) plots the histogram of the set of 76 contrasts shown in Table-5. Figure-26 right shows the cumulative histogram versus contrast obtained by integrating the histogram from 0 to the contrast value on the abscissa. Its interpretation is the fraction of contrasts at or below the given contrast and it represents the confidence curve. The theoretical cumulative PDF (blue curve) is also shown for 18 DOF (19 realizations – 1) for the mean and standard error in Table-5 lower right. The results in Table-5 (bottom 4 rows) also show that over the complete set of 76 realizations that the narrowband contrast at the 90% confidence level is $5.68 \times 10^{-9} \pm 8.76 \times 10^{-11}$. Figure-26 shows that the confidence curve and cumulative histogram yield this same contrast (0.90 on the “Cumulative Histogram” axis).

In section 4. *Success Criteria*, there are 3 criteria for assessing the success of the milestone and we have met these criteria as delineated here:

4.1: Illumination is narrowband light (<1% spectral bandpass) in a single linear polarization at a wavelength centered on 632.8 nm.

This has been accomplished and all the experiments and DCEs were performed using a broadband source with a narrowband spectral filter of FWHM = 1.2 nm centered on 632.8 nm.

4.2 The mean plus 1.33 of the standard error of the contrast is 1×10^{-8} or smaller at a pixel at $2 \lambda/D$, as reported in a Data Collection Event (DCE) spanning 1000 seconds of continuous data-taking containing 200 contrast estimates reported as a function of time.

Table-5: Milestone #1 Results

Realization	DCE-1 Contrast $\times 10^{-9}$	DCE-2 Contrast $\times 10^{-9}$	DCE-3 Contrast $\times 10^{-9}$	DCE-4 Contrast $\times 10^{-9}$
1	5.86	5.25	3.95	5.36
2	5.40	4.09	4.71	4.64
3	5.15	3.98	4.72	4.79
4	4.88	3.80	4.29	4.61
5	4.93	3.87	4.35	4.66
6	5.06	3.95	3.95	4.80
7	5.54	3.96	5.03	4.98
8	5.54	3.61	5.01	5.02
9	5.31	3.65	4.96	5.45
10	6.30	3.93	4.88	5.12
11	5.23	3.75	4.90	6.11
12	4.89	3.67	4.63	5.21
13	5.05	3.99	4.94	4.94
14	4.98	4.24	4.41	5.26
15	5.77	3.73	4.84	5.09
16	5.52	3.41	4.13	5.30
17	6.68	3.42	4.27	6.31
18	6.64	3.50	4.28	5.07
19	5.98	3.91	4.25	5.08
Ave: <C> =	5.51×10^{-9}	3.88×10^{-9}	4.55×10^{-9}	5.15×10^{-9}
Sigma: σ =	5.65×10^{-10}	3.99×10^{-10}	3.64×10^{-10}	4.46×10^{-10}
Std Error =	$\pm 1.30 \times 10^{-10}$	$\pm 9.16 \times 10^{-11}$	$\pm 8.35 \times 10^{-11}$	$\pm 1.02 \times 10^{-10}$
Students-t =	34.61	66.82	65.21	47.40
Confidence =	> 99.99 %	> 99.99 %	> 99.99 %	> 99.99 %
Average over all 76 realizations			4.77×10^{-9}	
Standard Dev (σ) over all 76 realizations			7.63×10^{-10}	
Standard Error over all 76 realizations			8.76×10^{-11}	
Contrast for 90% Confidence			5.68×10^{-9}	

Technology Advisory Committee. In the event that the success criteria have been met, the Program will submit the findings of the TAC, together with the certification data package, to NASA HQ for official certification of milestone compliance. In the event of a disagreement between the Program and the TAC, NASA HQ will determine whether to accept the data package and certify compliance or request additional work.

Table-5 shows that this effort significantly exceeded the 10^{-8} contrast at $2 \lambda/D$ to a confidence level of >99.99%. Additionally we showed average contrasts over the entire region of the dark-hole of $\sim 6 \times 10^{-8}$ into $1.5 \lambda/D$ inner working angle.

4.3 Elements 4.1 – 4.2 must be satisfied on three separate occasions with at least 24 hours between the beginnings of each demonstration.

These efforts exceeded element 4.2, with narrowband illumination per element 4.1, on four separate occasions separated by 1-day intervals. This is one more occasion (DCE) than was proposed at the outset of this effort. Thus the contrast is repeatable.

6. Certification Process

The Principal Investigator has assembled the milestone certification data package for review by the Exoplanet Exploration Program and its

6.1. Milestone Certification Data Package

The milestone certification data package is delivered with this report and contain the following: a spreadsheet with a brief summary and contrast statistics, and the set of contrast.

6.1.1. A narrative report, including a descriptive discussion of how the milestone was met, an explanation of each set of images, appropriate tables and summary charts, and a narrative summary of the overall milestone achievement – *this report and its accompanying spreadsheet serves that function.*

6.1.2. A description of the optical elements, their significant characteristics, and their layout and purpose in the VNC – *this is contained within this report.*

6.1.3. A dataset consisting of the set of raw contrast maps from the 4 DCE's. Each DCE will have reported 19 contrast maps images with suppression giving 76 contrast maps in all. Each image will be stored in a FITS file format in 512 x 512 x 4 byte floating point format or 1 MByte per contrast map giving overall 76 MBytes of data. *This data set is a gzipped tar file named Milestone1_VNC_TDEM_071213.tar.gz and is delivered with this report.* Additionally for each DCE, mean and standard deviation contrasts will be calculated and stored along with the dataset in the form of a spreadsheet. *This spreadsheet has been included with the deliver of this report and is named Milestone1_ContrastResults.xlsx. This aggregate set of contrast maps and deliverables has also been stored to a CD and archived. Further deliveries or distribution are available upon request.*

6.1.4. A tabulation of the significant operating parameters of the apparatus, including temperature stability and vibration environment.

6.1.5. A contrast metric value, as function of time, over each 1000-second DCE, for target areas of 2, 3, and 4 λ/D in the contrast image, in both tabular (spreadsheet) and in plotted form. *This is included in the delivered spreadsheet and within this document in tabular and textual form.*

6.1.6. Statistical data, including the contrast means and standard deviations for each of the 4 DCEs. *Included in this report and within the spreadsheet.*

6.1.7. Histograms of the contrast over the set of DCEs. *Included in this report.*

6.1.8. Additionally we had proposed, as ancillary data, to deliver a set of contrast maps with the shear setting optimized for IWA of 3 and 4 λ_0 / D , however these are not needed to meet the milestone and due to time constraints were not completed within the confines of this effort. *However, we did plot the contrasts from 1 to 6 λ/D and these contrast numbers are included in the spreadsheet delivered with this report.*

The aggregate dataset size delivered with this report is < 80 MBytes

7. Summary and Future Milestones

We claim worst- and best-case narrowband contrasts of $5.51 \times 10^{-9} \pm 1.30 \times 10^{-10}$ and $3.88 \times 10^{-9} \pm 9.16 \times 10^{-11}$ respectively, both to >99.99% confidence, at $2 \lambda/D$, over the set of 4 DCE confidences based on the results shown herein.

This was performed as a collaborative effort of M. Clampin, R. Lyon, P. Petrone, U. Mallik, M. Bolcar and M. Helmbrecht and each was actively engaged with this effort. The milestone is as discussed within this report and Figure-2 shows the context of this TDEM effort and milestone with regards to the past ASMC study, past and present technology development, past and present testbed efforts, and for future Milestones #2 and #3.

EPIC was proposed as a NASA Discovery proposal in 2006 and while not selected it did pass through a number of internal reviews at NASA/GSFC. It was later funded as a NASA ASMC study 2008 – 2009 which further defined the science case, mission architecture, instrument requirements and was independently costed through both GSFC Instrument Development Lab (IDL) and JPL's Team-X. During this time frame the specific technologies (yellow box middle left of Figure-2) were advanced through both IRAD, and SBIR Phase-I and II efforts, and a VNC testbed was developed at GSFC 1st in air and then in vacuum. In air it achieved broadband pupil nulling in visible light in 2008 and later suppression of the focused Airy disk core in vacuum. The combined testbed and IRAD and SBIR led to the development of the Vacuum Nuller Testbed (VNT) that has been used in this TDEM effort.

Following our current milestone achievement we expect to advance our next Milestone. This consists of inserting the spatial filter array (SFA) after the 2nd beamsplitter and achromatic phase shifters to achieve a VNC contrast of 10^{-9} contrast in 40 nm spectral bandpass in both polarization states simultaneously.

Milestone #2 requires the SFA. The SFA is a jointly funded effort between GSFC and JPL who both funded Fiberguide industries to develop it and it was delivered to GSFC in June of 2010. Separate versions were tested at both GSFC and JPL and both reached the conclusion that the lenslet arrays were misaligned. JPL and GSFC worked with the vendor to rectify this problem and the JPL version has now been properly aligned and separately tested at JPL. The GSFC version is currently undergoing re-alignment at Fiberguides facility in Idaho and expected to be delivered back to GSFC in early September. No TDEM funding was used for the SFA development effort. It consists of an array of coherent fibers sandwiched between two custom lenslet arrays, one input lenslet and one output lenslet per fiber. It is also known as a coherent fiber bundle. Each fiber is optically mapped to one MMA segment and it functions as a passive wavefront corrector since wavefront errors at the spatial frequency scale of one cycle per MMA segment and higher are not coupled into the fiber but shows up a small coupling loss (throughput loss). Additionally it functions in concert with the MMA to actively correct amplitude errors.

It also requires an achromatic phase shifter (APS) that effectively corrects the phase difference between the two arms of the nuller to π over a specified bandpass. Without the

APS the null is inherently narrowband due to the phase shift being set by the path length difference in the two arms of the nuller. The development of the APS has been separately funded under GSFC internal funds and two versions of it have been developed with a 3rd currently in progress.

Ultimately meeting all three milestones ensures that broadband and stable visible light high contrast imaging can be achieved to realize the EPIC mission. Additionally technologies developed under this effort are useful for other coronagraphic missions.

8. Glossary

ADU:	Analog to Digital Units to describe quantized counts output from detector.
APS:	Achromatic Phase Shifter consisting of optics to compensate pathlength to maintain constant phase ($\phi = 2\pi \cdot Pathlength/\lambda$) over wavelength band.
ARMA:	Auto-Regressive Moving Average
ASMC:	Astrophysics Strategic Mission Concept
BS:	Beamsplitter.
BOS:	Bright Object Sensor.
CCD:	Charge Coupled Device.
cpa:	Cycles per Aperture, used to refer to spatial frequencies.
DCE:	Data Collection Event.
DM:	Deformable Mirror.
DOF:	Degrees of Freedom.
EMCCD:	Electron Multiplying Charge Coupled Device.
EPIC:	Extrasolar Planetary Imaging Coronagraph, a proposed space mission for detecting and characterizing exosolar jovian planets and debris disks.
FITS:	Flexible Image Transport System, standardized file format for Astronomy.
FOV:	Field of View
HQ:	NASA Headquarters.
IDL:	NASA/GSFC Instrument Development Lab
IRAD:	Internal Research and Development.
IWA:	Inner Working Angle.
LOS:	Line of Sight.
mas:	Milli-arcseconds.
MEMS:	Micro Electrical Mechanical Structure.

MMA:	Multiple Mirror Array is a MEMS based mirror consisting of 2D array of hexagonal packed mirror segments, each actuated in piston, tip, and tilt.
MPI:	Message Passing Interface. Set of computer constructs for parallel coding.
NASA:	National Aeronautics and Space Administration.
NCB:	Null Control Breadboard. GSFC built white-light Michelson interferometer to test deformable mirrors and develop sensing & control.
ND:	Neutral Density. Used to describe an absorbing filter to attenuate light.
Nuller:	A single modified Mach-Zehnder nulling interferometer. The visible nulling coronagraph consists of two in series.
OSCAR:	Optical Systems Characterization and Analysis Research software, a suite of optical modeling software.
OTE:	Optical Telescope Element. The telescope portion of spacecraft for EPIC.
OWA:	Outer Working Angle.
PDF:	Probability Density Function.
PSF:	Point Spread Function. The spatial or angular spread of an unresolved source as imaged through an optical system.
RMS:	Root Mean Square.
RTOS:	Real Time Operating System.
SBIR:	Small Business Initiative Research.
SCI:	Dark Science focal plane.
SFA:	Spatial Filter Array consisting of a 2D array of coherent fibers with each fiber mated to an input and output lenslet, 2 lenslets per fiber.
STOP:	Structural Thermal Optical analysis.
TAC:	Technical Advisory Committee.
TDEM:	Technology Development for Exoplanet Missions.
TPF-C:	Terrestrial Planet Finger – Coronagraph.
VNC:	Visible Nulling Coronagraph.
VNT:	Vacuum Nuller Testbed, often referred to herein as Lab VNC, and is the testbed used in this TDEM effort to achieve Milestone #1.
WF:	Wavefront.
WFC:	Wavefront Control, usually refers to both wavefront sensing and control.
WFSC:	Wavefront Control, sensing and control.
WFE:	Wavefront Error used in an RMS sense to describe wavefront errors.

9. References

- [1] M. Clampin, R. Lyon, G. Melnick, D. Golimowski, H. Ford, J. Ge, G. Hartig, M. Harwit, G. Illingworth, S. Kendricks, B. M. Levine, D. Lin, M. Marley, L. Petro, J. Schneider (Obs-PM), D. Sasselov, S. Seager, S. Kenyon, M. Shao, W. Sparks, V. Tolls, A. Weinberger, R. Woodruff, *The Extrasolar Planetary Imaging Coronagraph: Architectures of Extrasolar Systems*, Final report to the NASA Astrophysics Strategic Concept Studies program, April 2009
- [2] R. G. Lyon, M. Clampin, R. A. Woodruff, G. Vasudevan, P. Thompson, P. Petrone, T. Madison, M. Rizzo, G. Melnick, V. Tolls, *Visible Nulling Coronagraph Testbed Development for Exoplanet Development*, Proc of SPIE 7731, (2010)
- [3] R. G. Lyon, M. Clampin, P. Thompson, T. Madison, R. Woodruff, G. Vasudevan, M. Rizzo, P. Petrone, G. Melnick, V. Tolls, *Visible Nulling Coronagraph Progress Report, Pathways Towards Habitable Planets*, Barcelona Spain (2009)
- [4] M. Clampin, R. Lyon and EPIC Science Team, *The Extrasolar Planetary Imaging Coronagraph*, Pathways Towards Habitable Planets, Barcelona Spain, Sept 14-18, 2009
- [5] Lyon, R.G., Clampin, M.C., Melnick, G.J., Tolls, V., Woodruff, R.A., Vasudevan, G., Rizzo, M., Thompson, P.L., *Visible Nulling Coronagraph Testbed Results*, Proc of SPIE 7440 (2009)
- [6] Richard G. Lyon, Mark Clampin, Gary Melnick, Volker Tolls, Robert Woodruff, Gopal Vasudevan, *Extrasolar Planetary Imaging Coronagraph: Visible Nulling Coronagraph Testbed Results*, Proceedings of SPIE Vol 7010, Marseille France, June 2008
- [7] R. G. Lyon, M. Clampin, M. Shao, R. Woodruff, G. Vasudevan, G. Melnick, V. Tolls, P. Petrone, *Nulling Coronagraphy for Exo-Planetary Detection and Characterization*, IAU #200, October 2005, Nice France
- [8] Y. Wen, B.J. Rauscher, R.G. Baker, M.C. Clampin, P. Fochi, S.R. Heap, G. Hilton, P. Jorden, D. Lindler, B. Mott, P. Pool, A. Waczynski, B. Woodgate, *Individual Photon Counting Using E2V L3 CCDs for Low Background Astronomical Spectroscopy*, Proc SPIE 6276, (2006)
- [9] C. C. Stark, M.J. Kuchner, *Detectability of Exo-Earths and Super-Earths Via Resonant Signatures in Exozodiacal Clouds*, ApJ 686 (2008)
- [10] P. de Groot, *Derivation of algorithms for phase-shifting interferometry using the concept of a data-sampling window*, Applied Optics, Vol. 34, Issue 22, pp. 4723-4730 (1995)
- [11] R.G. Lyon, M. Clampin, P. Petrone, U. Mallik, T. Madison, M.R. Bolcar, *High Contrast Vacuum Nuller Testbed (VNT) Contrast, Performance and Null Control*, Proc of SPIE 8442 (2012)

- [12] Yaitskova, N., Dohlen, K., Dierickx, P., *Analytical Study of Diffraction Effects in Extremely Large Segmented Telescopes*, JOSA **20**, No. 8, (2003)
- [13] Golub, G. H., and van Loan, C. F., *Matrix Computations*, The Johns Hopkins University Press, Third Edition (1996)
- [14] Grey, L., Lyon, R. G., *Correction of Misalignment Dependent Aberrations of the Hubble Space Telescope via Phase Retrieval*, Proc. SPIE, 1168 (1989)
- [15] Lyon, R. G., Miller, P. E., *Phase Retrieval Algorithms and Results*, Proc. of the First Hubble Aberration Recovery Program Workshop, Nov 15-16 (1990), R. Korechhoff ed. (JPL)
- [16] Lyon, R. G., Miller, P. E., Gruszczak, A., *Hubble Space Telescope Phase Retrieval: A Parameter Estimation*, Proc. of SPIE 1567 (1991)
- [17] Lyon, R. G., Hollis, J. M., Dorband, J. E., *Hubble Space Telescope Faint Object Camera Calculated Point Spread Functions*, Applied Optics, Vol. 36, No. 8 (1997)
- [18] Lyon, R. G., Hollis, J. M., Dorband, J., Murphy, T. P., *Extrapolating HST Lessons to NGST*, Optics and Photonics News, Vol. 9, No. 7 (1998)
- [19] Murphy, T. P., Lyon, R. G., Dorband, J. E., Hollis, J. M., *Sparse Matrix Approximation Method for an Active Optical Control System*, Applied Optics, Vol. 40, No. 35 (2001)
- [20] Lyon, R. G., Howard, E., Kaymaz, E., *Performance of Maximum Entropy Overresolution Algorithm*, AMOS Technical Conference, Maui Hawaii (2001)
- [21] Clampin, M., Ford, H. C., Lin, D. N. C., Lyon, R. G., Seager, S., Rauscher, B. J., Sparks, W. B., Petro, L., Tolls, V., Kuchner, M. J., Illingworth, G. D., Melnick, G. J., Weinberger, A., Marley, M., Shao, M., Kasting, J., Horner, S. D., Woodruff, R. A., *The Coronagraphic Exploration Camera (CorECam) Instrument Concept for TPF*, Proc. of SPIE 6265 (2006)
- [22] Clampin, M., Melnick, G., Lyon, R. G., Kenyon, S., Sasselov, D., Tolls, V., Ford, H., Golimowski, D., Petro, L., Hartig, G., *Extrasolar Planetary Imaging Coronagraph (EPIC)*, Proc. of SPIE 6265 (2006)
- [21] Lyon, R. G., Heap, S., Lo, A., Cash, W., Starkman, G., Vanderbei, R., Kasdin, J., Copi, C., *Externally Occulted Terrestrial Planet Finder Coronagraph: Simulation and Sensitivities*, Proc. of SPIE, Vol. 6687 (2007)